LIMNOLOGY
and
OCEANOGRAPHY: METHODS

Limnol. Oceanogr.: Methods 2, 2004, 262–281

Mapping coastal optical and biogeochemical variability using an autonomous underwater vehicle and a new bio-optical inversion algorithm

Catherine A. Brown[1], Yannick Huot[1], Michael J. Purcell[2], John J. Cullen[1], and Marlon R. Lewis[1]*

[1]Centre for Marine Environmental Prediction, Department of Oceanography, Dalhousie University, Halifax, Nova Scotia, B3H 4J1, Canada

[2]Woods Hole Oceanographic Institution, Department of Applied Physics and Ocean Engineering, MS 10, Woods Hole, MA 02543, USA

Abstract

Autonomous underwater vehicles (AUVs) can map water conditions at high spatial (horizontal and vertical) and temporal resolution, including under cloudy conditions when satellite and airborne remote sensing are not feasible. Applications of this technology are numerous, and harnessing the full potential of AUV platforms for oceanographic research will require innovative sampling and data processing techniques, particularly in shallow littoral environments. We deployed a passive radiometer on a small AUV called the Remote Environmental Monitoring UnitS (REMUS; Hydroid) to demonstrate a novel method that uses one optical sensor at depth to characterize variability in underwater clarity and the constituents of coastal seawater (i.e., dissolved organic material, algal biomass, and other particles). This approach uses spectral differences between attenuation coefficients that are computed from ratios of downwelling irradiance measured at one depth assuming a constant shape, but not magnitude, for the solar irradiance spectrum at the surface. A spectral inversion model provides estimates of the absorption coefficients (m^{-1}) of the constituents above the sensor. There is no requirement for sensors at the ocean surface using this approach and, compared to inversion methods for subsurface reflectance, the effects of bottom reflectance in shallow waters are minimal. Maps of bio-optical properties at high spatial resolution demonstrate that our approach can be used for characterizing shallow and highly variable coastal waters. This simple and robust technique is also applicable to other in situ sampling platforms (e.g., gliders, moorings, Argo floats).

Satellite and airborne observations of oceanic optical properties allow synoptic views of the ocean but are infrequent and often contaminated by clouds. On the other hand, stationary in situ sensors provide high temporal resolution independent of cloud cover (e.g., Zheng et al. 2002), but do not provide a spatial context unless deployed as an array (Abbott et al. 2000). The recent development of small, comparatively low-cost, long-range autonomous underwater vehicles (AUVs) provides an ideal sensor platform for resolving both spatial and temporal variability, and for permitting adaptive sampling of the ocean given the capability for a variety of flight patterns (e.g., Glenn et al. 2000; Griffiths et al. 2001; Griffiths 2002; Rudnick and Perry 2003). The addition of optical sensors onto submersible vehicles has opened new doors to the exploration of optical variability in the sea (Yu et al. 2002). The potential for AUVs to provide new insight into the ocean environment is clear; however, the broad use of this technology by the ocean science community is dependent upon cost-effective and robust sampling methodologies. Here, we demonstrate the use of an AUV to map optical and physical properties of the littoral ocean in two and three dimensions. We decompose the observed optical signal into its contributions from various seawater constituents using a new bio-optical algorithm, thereby providing a rapid and accurate means for mapping

*E-mail: cbrown9@dal.ca

Acknowledgments

We are grateful to Trisha Bergmann and Mark Moline for providing the in situ measurements of IOPs. We thank Emmanuel Boss and Mark Moline for thorough comments on an earlier version of the manuscript. We also thank an anonymous reviewer for comments, which helped to improve the manuscript. This work was supported by the U.S. Office of Naval Research under the HyCODE and Environmental Optics programs and the Natural Sciences and Engineering Research Council (Canada) under Operating Grants and Research Partnerships Grants. C.A. Brown was supported by a Killam Memorial Fellowship, the Office of Naval Research, and the Canadian Foundation for Climate and Atmospheric Sciences, the latter of which also provided support to Y. Huot.

Table 1. List of symbols, definitions, and units

Symbol	Definition	Unit
$a(\lambda,z)$	Total absorption coefficient	m^{-1}
$\bar{a}^0(\lambda,z_{AUV})$	Total absorption coefficient between the surface and z_{AUV} retrieved from $\delta K_d^0(\lambda,z_{AUV})$	m^{-1}
$a_{cm}(\lambda,\bar{z})$	Absorption coefficient for nonalgal colored matter computed for a small (1 to 3 m) depth interval	m^{-1}
$\bar{a}_{cm}^0(412,z_{AUV})$	Absorption coefficient for nonalgal colored matter at 412 nm between the surface and z_{AUV} retrieved from $\delta K_d^0(\lambda,z_{AUV})$	m^{-1}
$a_{ph}(\lambda,\bar{z})$	Absorption coefficient for phytoplankton computed for a small (1 to 3 m) depth interval	m^{-1}
$\bar{a}_{ph}^0(522,z_{AUV})$	Phytoplankton absorption coefficient at 522 nm (corresponds to the average value from 400 to 700 nm) between the surface and z_{AUV} retrieved from $\delta K_d^0(\lambda,z_{AUV})$	m^{-1}
$\tilde{a}_{ph}(\lambda)$	Mean normalized phytoplankton absorption coefficient with a size factor of 0.25	Dimensionless
$a_w(\lambda)$	Absorption coefficient for pure seawater	m^{-1}
$b_b(\lambda,z)$	Total backscattering coefficient	m^{-1}
$\bar{b}_b^0(\lambda,z_{AUV})$	Total backscattering coefficient between the surface and z_{AUV}	m^{-1}
Chl	Chlorophyll *a* concentration	mg m^{-3}
$E_d(\lambda,z)$	Downwelling irradiance	W m^{-2} nm^{-1} or µmol m^{-2} s^{-1} nm^{-1}
$K_d(\lambda,z)$	Diffuse attenuation coefficient for downwelling irradiance	m^{-1}
$K_d(\lambda,\bar{z})$	$K_d(\lambda,z)$ computed for a small (1 to 3 m) depth interval	m^{-1}
$\bar{K}_d^0(\lambda,z_{AUV})$	Average $K_d(\lambda)$ between the surface and z_{AUV}	m^{-1}
$\delta\bar{K}_d^0(\lambda,z_{AUV})$	Spectral differences between $\bar{K}_d^0(\lambda,z_{AUV})$	m^{-1}
$\delta K_d(\lambda)$	Spectral differences of $K_d(\lambda,\bar{z})$	m^{-1}
PAR	Photosynthetically active radiation $\left(=\int_{400}^{700} E_d(\lambda)d\lambda\right)$	µmol m^{-2} s^{-1}
$S_{<f>}$	Size factor for phytoplankton absorption spectrum	Dimensionless
z	Depth	m
z_{AUV}	Depth of the AUV	m
$\bar{z}$	Average depth of the small depth interval used to calculate $K_d(\lambda,\bar{z})$ and $\delta K_d(\lambda)$	m
$\bar{\mu}_d(\lambda,z)$	Average cosine for the downwelling radiance distribution	Dimensionless

and predicting biogeochemical variability in coastal waters. The challenge lies in the interpretation of the observed light field in terms of optical and biological constituents. In the coastal zone, where terrigenous runoff and bottom reflectance complicate optical signatures, this interpretation is not trivial.

Bases—The constituents of seawater (i.e., phytoplankton, colored dissolved materials, nonalgal particulates) influence the fate of solar energy in the ocean. It follows that observations of reflectance (the ratio of upwelling radiance to downwelling irradiance) or the attenuation of downwelling irradiance can be used to diagnose components of environmental variability in the sea (Dickey 1991; Cullen et al. 1997; Dickey and Chang 2001; Sosik et al. 2001). Here, we focus on measurements of spectral downwelling irradiance and the description of its attenuation with depth. An advantage of measuring irradiance is that absolute calibrations of radiometers can be performed with U.S. National Institute of Standards and Technology (NIST), or NIST-traceable, lamps using International Organization for Standardization procedures; measurements taken at particular locations and times can be unambiguously compared with observations taken at any other place or time. A large effort by the community has resulted in an extensive series of protocols governing the characterization and calibration of sensors to measure these quantities with a high degree of confidence (2% absolute, Mueller and Fargion 2002).

Given measurements of downwelling irradiance as a function of depth, we compute an apparent optical property (Preisendorfer 1976), the diffuse attenuation coefficient,

$$K_d(\lambda,z) = -\frac{d\ln E_d(\lambda,z)}{dz} = -\frac{1}{E_d(\lambda,z)}\cdot\frac{dE_d(\lambda,z)}{dz} \quad (1)$$

where $E_d(\lambda,z)$ is the ambient downwelling spectral irradiance (W m^{-2} nm^{-1}) at depth z (m), and $K_d(\lambda,z)$ is the diffuse attenuation coefficient for downwelling irradiance (m^{-1}) (*see* Table 1 for a summary of symbols, definitions, and units). The $K_d(\lambda,z)$ can then be expressed in terms of contributions from known sources of optical variability (Kirk 1994). For example, in

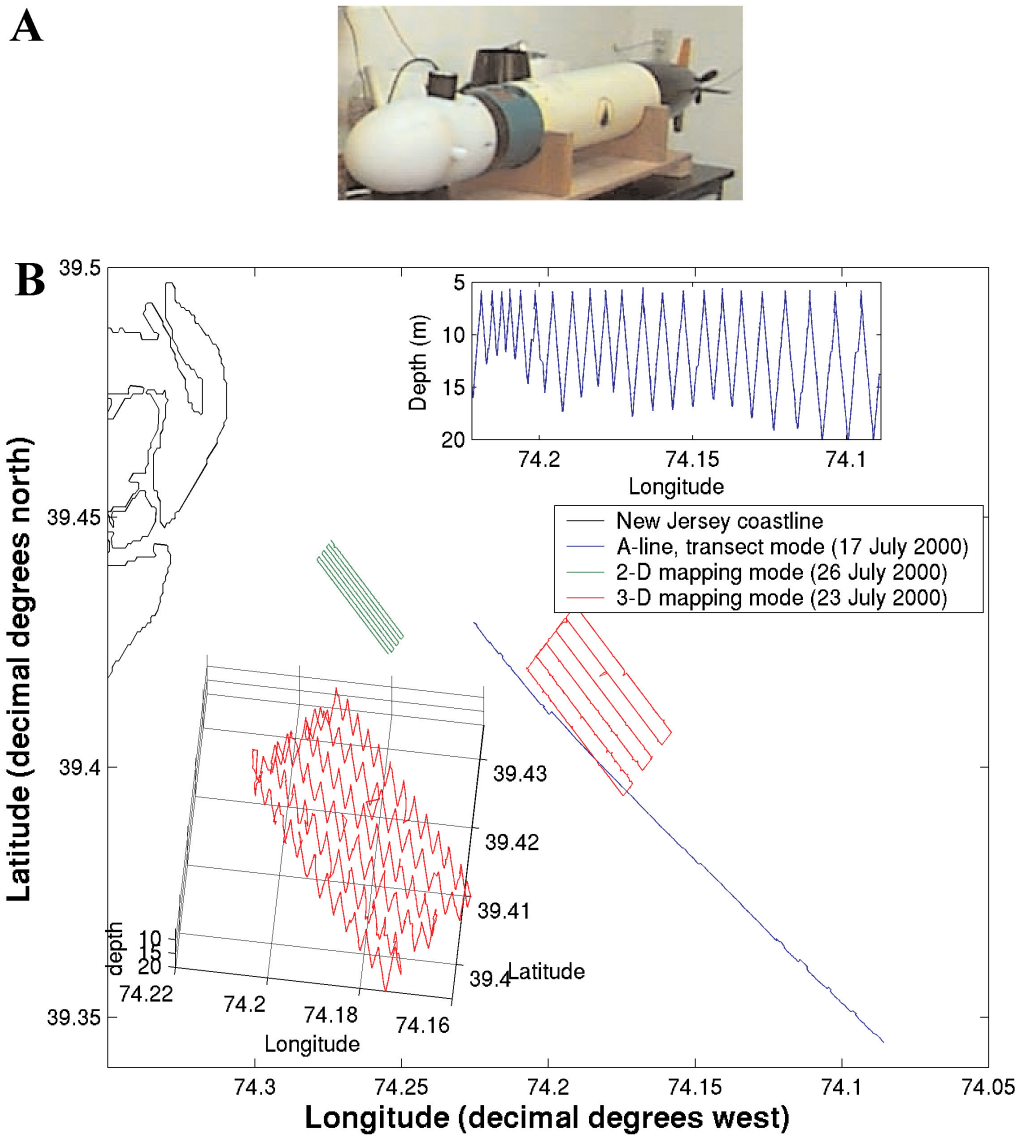

Fig. 1. The REMUS and a map of the study region. (A) The REMUS (160 cm long with 19 cm diameter) was outfitted with an optical sensor payload for this study. The irradiance sensor head (Satlantic) is shown positioned fore on the submersible. (B) The study area and REMUS sampling patterns. The upper subset shows the depth profile in transect mode while the lower subset shows the depth profile in 3-D mode. In transect mode, REMUS followed the 'A-line' at the LEO study site.

Case 1 waters the chlorophyll *a* concentration (Chl, mg m^{-3}) can be estimated from observations of $K_d(\lambda,z)$ using simple empirical relationships (Morel 1988; Bricaud et al. 1998; Morel and Maritorena 2001), much as Chl is obtained from reflectance ratios in remote sensing applications. More complex models include contributions from other constituents such as colored dissolved organic matter (CDOM), suspended sediment, or bubbles (e.g., Roesler and Perry 1995; Carder et al. 1999; Ciotti et al. 2002; Maritorena et al. 2002; Zhang et al. 2002).

We use the spectral attenuation of downwelling light, rather than reflectance, in our analysis for four reasons: (1) coastal waters often contain high amounts of CDOM, which is highly absorbing at short wavelengths, thus reducing the depth at which upwelling radiance is available at the wavebands needed (i.e., < 440 nm) to accurately estimate the amount of CDOM; (2) in shallow waters, bottom reflectance can strongly affect measurements of reflectance (e.g., Albert and Mobley 2003); (3) in most open ocean and coastal waters, attenuation is weakly influenced by backscattering, and thus its accurate parameterization is not as critical as for inverse models of reflectance (Roesler and Boss 2003); and (4) only one sensor is required to measure the downwelling light field, whereas two are needed to measure reflectance.

$K_d(\lambda,z)$ can be approximated in the following manner (Gordon 1989):

$$K_d(\lambda,z) \approx \frac{a(\lambda,z)+b_b(\lambda,z)}{\bar{\mu}_d(\lambda,z)} \quad (2)$$

where $a(\lambda,z)$ is the total absorption coefficient (m^{-1}), $b_b(\lambda,z)$ is the total backscattering coefficient (m^{-1}), and $\bar{\mu}_d(\lambda,z)$ is the mean cosine of the downwelling radiance distribution (dimensionless). The absorption and backscattering coefficients are inherent optical properties (IOPs; i.e., properties that depend only on the medium, and therefore are independent of the radiance distribution within the medium; Preisendorfer 1976). The value of $\bar{\mu}_d(\lambda,z)$ carries information on the angular distribution of the incident radiance, which changes with sun angle, the proportion of diffuse to direct light, sea-state, and modifications of the radiance field caused by scattering in the sea (Kirk 1994; Berwald et al. 1998). Within reasonable accuracy, for solar zenith angles less than 60° and at least for blue-green wavelengths in most open ocean environments, variations in $\bar{\mu}_d(\lambda,z)$ can be estimated, thus allowing the retrieval of $a(\lambda,z)$ (and potentially $b_b(\lambda,z)$, if sufficiently high relative to $a(\lambda,z)$) from measurements of $K_d(\lambda,z)$, a property that has been described as quasi-inherent (Baker and Smith 1979; Zheng et al. 2002).

The estimation of $K_d(\lambda,z)$ can be made with two or more calibrated sensors by measuring $E_d(\lambda,z)$ simultaneously at various depths. It can also be estimated by measuring $E_d(\lambda,z)$ at a fixed depth or in vertical profile while measuring downwelling irradiance at the sea surface to account for variability in the incident solar irradiance field. The use of a surface sensor is impractical in the case of an AUV, and this prevents the direct derivation of $K_d(\lambda,z)$ from the sea surface to the depth of the sensor. An alternative method, employed with profiling radiometers when a surface reference is unavailable, is to estimate $K_d(\lambda,z)$ using a single sensor by varying its depth (e.g., Mitchell et al. 2000), assuming that variation in the incident solar flux at the sea surface during the measurement is small by comparison to the attenuation of energy over the depth interval.

The retrieval of chlorophyll concentration and yellow substance absorption at 440 nm from light attenuation data have been applied to vertical profiles of $E_d(\lambda)$ without requiring a reference sensor at the surface (Nahorniak et al. 2001). With this method, profiles of the spectrum of downwelling irradiance normalized to one waveband are used to obtain spectral K_d differences, and a semi-empirical algorithm for the retrieval of the constituents is then carried out. This approach has the advantage of being independent of changes in the magnitude of the light field at the surface. In this study, we use a similar approach but have removed the need for irradiance profiles by making an assumption regarding the spectral shape of the surface irradiance. In addition, we have replaced the use of a semi-empirical model by an inverse model, which we believe to be more suitable for Case 2 waters (i.e., waters for which the optical properties do not covary strongly with phytoplankton biomass, usually because of a strong influence of inorganic particles and CDOM), where regional empirical algorithms have not yet been developed. This method is applicable to $E_d(\lambda,z)$ measurements from a wide variety of platforms (e.g., AUVs, profilers, floats, gliders, moorings) for the mapping and monitoring of optical and biogeochemical variability in coastal and open ocean waters.

Materials and procedures

Observing platform and sensor payload—The Remote Environmental Monitoring UnitS (REMUS; Hydroid) is an AUV originally developed by the Oceanographic Systems Laboratory at Woods Hole Oceanographic Institution (Purcell et al. 2000). This lightweight (37 kg in air) and compact submersible is specifically designed for underwater mapping in littoral environments; it is a torpedo-shaped device with a diameter of 19 cm and a length of 160 cm (Fig. 1). The vehicle is programmed to follow a preplanned mission path in both the horizontal and vertical, and navigates using a combination of long baseline and dead-reckoning with compass and velocity logs. The range in velocity is approximately 0.25 to 2.8 m s^{-1}. At an optimal velocity of 1.5 m s^{-1}, the vehicle endurance is ~22 h.

For this study, REMUS was deployed with a payload consisting of a Conductivity-Temperature-Depth sensor (CTD; Ocean Sensors), an active chlorophyll fluorometer (WETStar, WET Labs), and a passive optical sensor head that measured $E_d(\lambda)$ (Satlantic). The radiometer has 7 independent channels centered at 412, 443, 490, 510, 555, 670, and 683 nm, all with half maximum bandwidths of 10 nm. The absolute accuracy of the irradiance measurements is within 2%, although variations in the vehicle's attitude (pitch and roll) may result in departures from the ideal case where the sensors are parallel with the ocean surface. For the deployments described here, the measured attitude of the AUV resulted in departures less than 6° for more than 94% of the mission, and always less than 8°; this is well within the limit of 10° recommended by the SeaWiFS protocols (Mueller and Fargion 2002) and hence, the error will be small. The sampling frequency of the radiometer was 1 Hz during the deployments. Sun-induced chlorophyll fluorescence (Maritorena et al. 2000) and Raman scattering (Marshall and Smith 1990) strongly influence $K_d(670)$ and $K_d(683)$; in addition, water itself has a high absorption at red wavelengths, thus we will not use these wavelengths in our inversion analysis.

Three basic mission modes can be selected for the AUV trajectory (*see* Fig. 1B): (1) in transect mode, the AUV travels a vertical sawtooth pattern along a straight line transect; (2) in two-dimensional (2-D) mapping mode, REMUS transits a radiator pattern while maintaining a relatively constant depth; and (3) in three-dimensional (3-D) mapping mode, the AUV travels a radiator pattern while undulating with depth. Deploying REMUS in transect mode allows the description of a vertical cross-section of water. In 2-D mapping mode, the area is

Table 2. Various methods for the calculation of light attenuation and corresponding REMUS deployment modes

Method	REMUS mode	Variables retrieved	Depth plotted
$K_d(\lambda,\bar{z})$, #1	Transect	$a_{ph}(\lambda)$, $a_{cm}(\lambda)$	$\bar{z} = z + 1/2 \cdot \Delta z$
$K_d(\lambda,\bar{z})$, #1	3-D mapping	none	$\bar{z} = z + 1/2 \cdot \Delta z$
$\delta\bar{K}_d^0(\lambda, z_{AUV})$, #2	Transect	$\bar{a}_{ph}^0(\lambda)$, $\bar{a}_{cm}^0(\lambda)$	z_{AUV}
$\delta\bar{K}_d^0(\lambda, z_{AUV})$, #2	2-D horizontal mapping	$\bar{a}_{ph}^0(\lambda)$, $\bar{a}_{cm}^0(\lambda)$	z_{AUV}
$\delta K_d(\lambda,\bar{z})$, #3	Transect	$a_{ph}(\lambda)$, $a_{cm}(\lambda)$	$\bar{z} = z + 1/2 \cdot \Delta z$

mapped in two horizontal dimensions. Three-dimensional mapping mode allows the description of the 3-D structure of the water volume.

In the following sections, we describe three methods that we used to analyze the downwelling irradiance data from the AUV.

Method 1: Calculation of $K_d(\lambda)$ over small depth intervals—During transect mode and 3-D mapping mode (Table 2), computations were made of the attenuation coefficient during both ascent and descent of the vehicle. Over a depth interval, Δz, the spectral irradiance decreases as

$$E_d(\lambda, z+\Delta z) = E_d(\lambda, z) \cdot \exp\left[-\bar{K}_d(\lambda,\bar{z}) \cdot \Delta z\right] \quad (3)$$

where $\bar{K}_d(\lambda,\bar{z}) = \frac{1}{\Delta z}\int_z^{z+\Delta z} K_d(\lambda, z) \cdot dz$, and $\bar{z} = z + 1/2 \cdot \Delta z$ is the depth assigned to $\bar{K}_d(\lambda)$ in our analysis. This approach assumes that surface irradiance does not vary over the time interval between observations at z and Δz. Over small depth intervals, we assume as well that $K_d(\lambda,z)$ does not vary significantly, and henceforth, we use the symbol $K_d(\lambda,\bar{z})$ to represent $\bar{K}_d(\lambda,\bar{z})$. Before calculating $K_d(\lambda,\bar{z})$, the optical data required preliminary processing. Appropriate dark values were identified for each wavelength as the value of $E_d(\lambda,z)$ when $\ln(E_d(\lambda,z))$ no longer changed linearly with depth, and were then subtracted from all $E_d(\lambda,z)$ measurements. In addition, a minimum $E_d(\lambda)$ value was chosen for each wavelength as a quality control cutoff representing when the signal was too low for accurate detection. The estimates of $K_d(\lambda,\bar{z})$ were then performed by linear regression of the log transformed $E_d(\lambda,z)$ data over 1- to 3-m depth intervals representing 30 $E_d(\lambda,z)$ measurements (the average ascent/descent rate was ~0.055 m s^{-1}). The $K_d(\lambda,\bar{z})$ values for which the fit had a correlation coefficient lower than 0.7 were excluded from the analysis. To create 2-D contour plots, the measured $K_d(\lambda,\bar{z})$ data were gridded onto Cartesian coordinates using Delaunay triangulation (a component of the standard MATLAB® software package) and a cubic interpolation scheme; here longitudinal variations are reported.

The inversion of $K_d(\lambda,\bar{z})$ to obtain $a_{ph}(522,\bar{z})$ and $a_{cm}(412,\bar{z})$—As described in Eq. 2, $K_d(\lambda,\bar{z})$ is a function of the absorption and backscattering coefficients, as well as the mean cosine ($\bar{\mu}_d$). For this study, we assumed that $\bar{\mu}_d$ was equal to 0.8 and independent of wavelength and optical depth. In the waters sampled, the backscattering from particles was small (less than 6% of the absorption coefficient at 488 nm) and was not included in the inversion analysis such that we made the approximation $K_d(\lambda,\bar{z}) \approx a(\lambda,\bar{z})/\bar{\mu}_d$. The absorption coefficients to be retrieved are average values for each 1- to 3-m depth interval over which $K_d(\lambda,\bar{z})$ is computed.

Consistent with the inverse modeling approach of Roesler and Perry (1995), the total absorption coefficient is represented as the sum of the absorption coefficients for the major absorbing components of seawater in the visible:

$$\begin{aligned} a(\lambda,\bar{z}) &= a_w(\lambda) + a_{ph}(\lambda,\bar{z}) + a_{cm}(\lambda,\bar{z}) \\ &= a_w(\lambda) + a_{ph}(522,\bar{z}) \cdot \tilde{a}_{ph}(\lambda) + a_{cm}(412,\bar{z}) \cdot \exp\left[-0.011 \cdot (\lambda - 412)\right] \end{aligned} \quad (4)$$

where $a_w(\lambda)$, $a_{ph}(\lambda,\bar{z})$, and $a_{cm}(\lambda,\bar{z})$ are the absorption coefficients (m^{-1}) for pure seawater (Pope and Fry 1997), phytoplankton, and nonalgal colored matter, respectively. The parameter $a_{ph}(522,\bar{z})$ is the algal absorption coefficient (m^{-1}) at 522 nm. The term $\tilde{a}_{ph}(\lambda)$ is the spectrum for a phytoplankton absorption coefficient with a size factor of 0.25 ($S_{<f>}$ as in Ciotti et al. 2002) normalized to the average value of the spectrum over the wavelength interval 400 to 700 nm, which corresponds to the value at 522 nm (dimensionless). For reference, using this spectrum $a_{ph}(412) = 2.1 \cdot a_{ph}(522)$ and $a_{ph}(490) = 1.7 \cdot a_{ph}(522)$. The $S_{<f>}$ is a linear mixing parameter between the normalized absorption spectrum for small cells ($S_{<f>} = 1$) and that of large cells ($S_{<f>} = 0$). A $\tilde{a}_{ph}(\lambda)$ spectrum with $S_{<f>} = 0.25$ represents a community dominated by large cells and/or cells with highly packaged pigments. A $S_{<f>}$ of 0.25 best represents the median phytoplankton absorption spectrum for 40 water samples taken between the surface and 9 m in the same region as our deployment within 9 d of the AUV deployments (data not shown, provided by Mark Moline pers. comm. 2003). The parameter $a_{cm}(412,\bar{z})$ is the absorption coefficient (m^{-1}) for nonalgal colored matter at 412 nm. The component $a_{cm}(\lambda,\bar{z})$ includes absorption due to CDOM and nonalgal particulates (i.e., detritus), both of which exhibit exponential decrease in absorption with wavelength. The slope of the exponential decline in the absorption coefficient for nonalgal colored matter is taken to be 0.011 nm^{-1}. This value matches the slope between 412 and 555 nm of the median of 40 absorption spectra of CDOM plus detritus sampled at the same time and location as the phytoplankton absorption spectra (data not shown, provided by Mark Moline pers. comm. 2003).

Table 3. Normalized subsurface irradiance spectra $\left[\frac{E_d(\lambda,0^-)}{E_d(490,0^-)}\right]$ used in the calculation of $K_d(\lambda,\bar{z})$ in Method 2*

REMUS mode	412 nm	443 nm	490 nm	510 nm	555 nm
Transect	0.87	0.98	1.00	1.00	0.98
2-D horizontal mapping	0.99	1.06	1.00	0.98	0.92

*These spectra include the spectral cloud effect (*see* text).

The inverse model uses a bounded nonlinear least squares method (Coleman and Li 1994, 1996) to simultaneously fit model parameters in Eq. 4 (i.e., $a_{ph}(522,\bar{z})$ and $a_{cm}(412,\bar{z})$), which represent the magnitudes of the various sources of spectral absorption. Although a linear least squares method would achieve the same results for our inversion algorithm, by using a nonlinear approach during its development we were able to compare different models for the inversion. The least squares convergence was robust and was not found to be sensitive to the magnitude of the initial values within their normal range. The maximum bounds for all parameters were set such that they never limited the fits, and all lower bounds were set to 0. By allowing the inversion algorithm to simultaneously fit the parameters, we can obtain the individual optical contributions from various constituents, subject to the simplifications used in this analysis. In the transect mode example, the inverse model uses $K_d(\lambda,\bar{z})$ at 412, 443, 490, 510, and 555 nm as input.

The method described above is applicable to deployments where the AUV undulates with respect to depth; here, this would be the case for both the transect mode and the 3-D mapping mode. Note that our deployment in 3-D mapping mode was on a day with thick cloud cover and very few values of $E_d(412,z)$ for this transect passed our quality control step (i.e., $E_d(412,z)$ was usually below our minimum cutoff value) due to the very low surface light levels and the high attenuation coefficient of the water. We thus decided to remove 412 nm from the 3-D mapping mode analysis, which results in high uncertainty in the separation of $a_{ph}(\lambda,\bar{z})$ from $a_{cm}(\lambda,\bar{z})$. Therefore, no inversion was attempted for this deployment, and we report only the three dimensional variation in the absolute values of $K_d(\lambda,\bar{z})$.

To summarize our inversion algorithm for $K_d(\lambda,\bar{z})$ (Method 1), once values for K_d are obtained, we minimize the following sum:

$$\sum_{\lambda}\left(K_d(\lambda,\bar{z})\cdot\bar{\mu}_d-\left\{a_w(\lambda)+a_{ph}(522,\bar{z})\cdot\bar{a}_{ph}(\lambda)+a_{cm}(412,\bar{z})\cdot\exp\left[-0.011\cdot(\lambda-412)\right]\right\}\right)^2$$

by allowing $a_{ph}(522,\bar{z})$ and $a_{cm}(412,\bar{z})$ to vary and setting $\bar{\mu}_d$ to 0.8. An interior-reflective Newton method was used in the least squares minimization algorithm (Coleman and Li 1994, 1996).

Method 2: Derivation of $\delta\bar{K}_d^0(\lambda,z_{AUV})$ *using an assumed surface spectrum*—During 2-D mapping mode, the AUV remains at a fixed depth while executing a survey with a radiator pattern. It is not possible to estimate $K_d(\lambda,\bar{z})$ as in Method 1, because the vertical gradient of downwelling irradiance is not measured, nor is it possible to estimate a vertically averaged $K_d(\lambda,z)$ between the sea surface and the depth of the AUV because no surface reference is available. The following method uses spectral ratios of irradiance measured at one depth and an assumed normalized spectrum of irradiance at the surface (Table 3). With this approach we obtain spectral differences in $\bar{K}_d^0(\lambda,z_{AUV})$, which is the average $K_d(\lambda)$ between the surface and the depth of the AUV (i.e., $\bar{K}_d^0(\lambda,z_{AUV})=\frac{1}{z_{AUV}}\int_{0-}^{z_{AUV}}K_d(\lambda,z)dz$), where the overbar refers to the average taken from the surface to the depth of the AUV and the 0 superscript indicates the use of the normalized surface irradiance spectrum in this method.

The sensor wavelengths used in the following analysis are 412, 443, 490, 510, and 555 nm. Irradiance values at each wavelength were normalized by $E_d(490,z_{AUV})$:

$$\frac{E_d(\lambda,z_{AUV})}{E_d(490,z_{AUV})}=\frac{E_d(\lambda,0^-)\cdot\exp\left[-\bar{K}_d^0(\lambda,z_{AUV})\cdot z_{AUV}\right]}{E_d(490,0^-)\cdot\exp\left[-\bar{K}_d^0(490,z_{AUV})\cdot z_{AUV}\right]} \quad (5)$$

where 0^- refers to the depth just below the surface. Rearranging and taking the logarithm of both sides to obtain spectral differences of $\bar{K}_d^0(\lambda,z_{AUV})$:

$$\delta\bar{K}_d^0(\lambda,z_{AUV})=\bar{K}_d^0(\lambda,z_{AUV})-\bar{K}_d^0(490,z_{AUV})=-\frac{1}{z_{AUV}}\cdot\ln\left[\frac{E_d(490,0^-)}{E_d(\lambda,0^-)}\cdot\frac{E_d(\lambda,z_{AUV})}{E_d(490,z_{AUV})}\right]. \quad (6)$$

The differences of attenuation coefficient between wavelengths are obtained without the explicit calculation of $\bar{K}_d^0(\lambda,z_{AUV})$. The ratio $E_d(\lambda,0^-)/E_d(490,0^-)$(*see* Table 3 for values used in this study) was computed using the clear sky model of Gregg and Carder (1990), accounting for the spectral effect of clouds if necessary. Although the spectral shape of the incident solar spectrum shows little variability under sunny conditions, for overcast conditions the spectral effect of clouds on the solar spectrum has been described (e.g., Bartlett et al. 1998; Siegel et al. 1999). In this study, it was cloudy during both the transect and 2-D mode deployments, and we accounted for the spectral cloud effect following Bartlett et al. (1998). For the cloud factor, we used the measured ratio of photosynthetically active radiation (PAR; *see* http://marine.rutgers.edu/cool/hycode/data/calendar.html for PAR measurements recorded at Long-term Ecosystem Observatory (LEO) in July 2000) above the sea surface on a given day to PAR for clear sky conditions, which was a substitute for $E_d(490,0^+)$ used by Bartlett et al. (1998). The day corresponding to the 2-D mode deployment was extremely

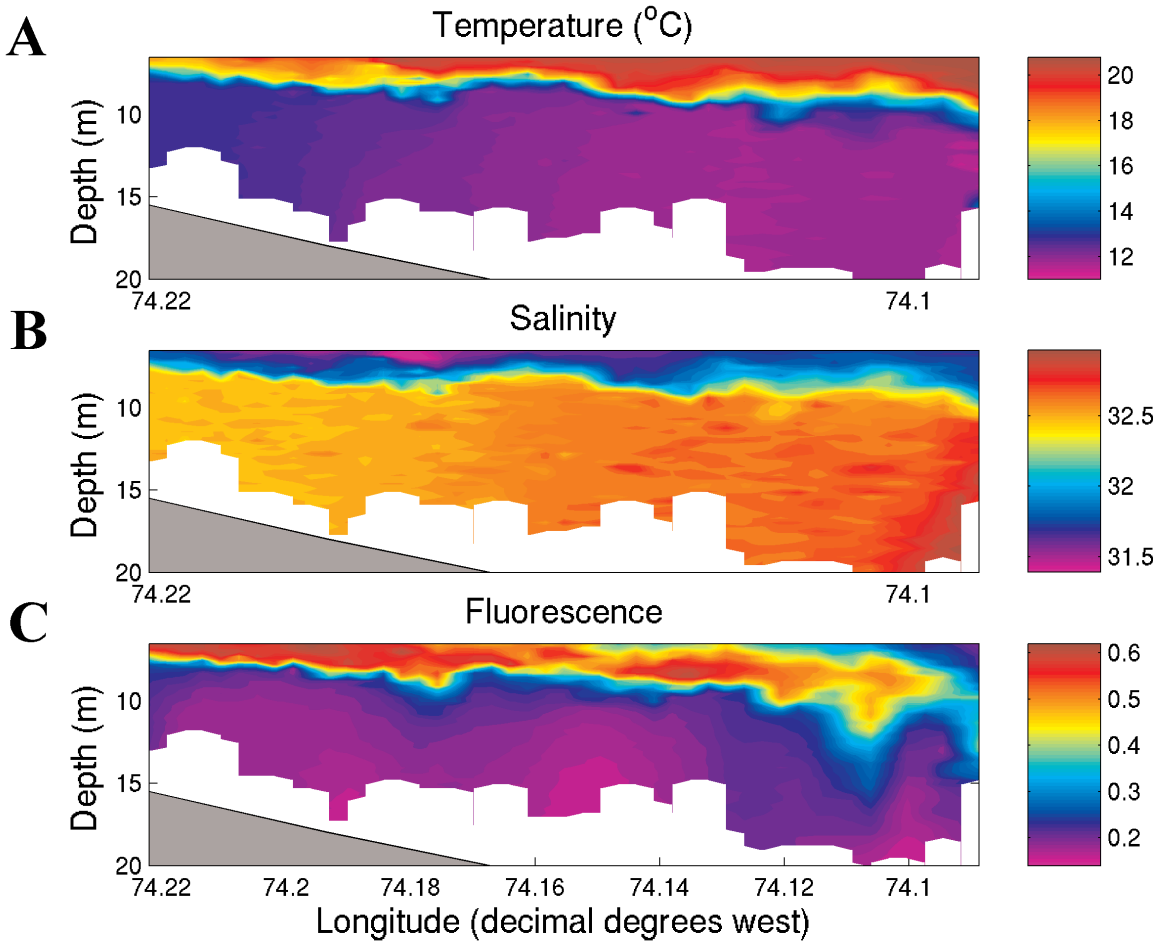

Fig. 2. Observations by instruments mounted on REMUS along the A-line transect. (A) temperature (°C); (B) salinity; (C) fluorescence (normalized to the maximum value for all deployments). The water is strongly stratified and the phytoplankton biomass is mostly restricted to the top 8 m.

overcast: the PAR irradiance was only ~17% of a sunny day. For the transect mode deployment, the PAR irradiance was ~80% of a sunny day. As shown here, under overcast skies the spectral effect of clouds can be accounted for by using a surface irradiance sensor (e.g., PAR or $E_d(490)$ sensor) near the deployment site. We did not account for the small difference in spectral transmission across the air-sea interface for a clear sky versus a cloudy sky.

For this analysis, we use z_{AUV} as the position when plotting $\delta\bar{K}_d^0(\lambda, z_{AUV})$. As such, a contour plot of $\delta\bar{K}_d^0(\lambda, z_{AUV})$ will represent the average values of $\delta\bar{K}_d^0(\lambda, z_{AUV})$ above the actual depth plotted. Whereas the $\delta\bar{K}_d^0(\lambda, z_{AUV})$ method is the only available option for 2-D mapping mode (i.e., AUV at a fixed depth), it can also be equally applied to transect mode and 3-D mapping mode (i.e., AUV undulating with respect to depth).

Inversion of $\delta\bar{K}_d^0(\lambda, z_{AUV})$ *to obtain* $\bar{a}_{ph}^0(522, z_{AUV})$ *and* $\bar{a}_{cm}^0(412, z_{AUV})$—The inverse model uses a nonlinear least squares method to simultaneously fit model parameters, $\bar{a}_{ph}^0(522, z_{AUV})$ and $\bar{a}_{cm}^0(412, z_{AUV})$, similar to the model described above for absolute measurements of $K_d(\lambda, \bar{z})$. However, in this analysis the inverse model uses $\delta\bar{K}_d^0(\lambda, z_{AUV})$:

$$\begin{aligned}\delta\bar{K}_d^0(\lambda, z_{AUV}) &= \bar{K}_d^0(\lambda, z_{AUV}) - \bar{K}_d^0(490, z_{AUV}) \\ &\approx \frac{1}{\bar{\mu}_d}\left(\bar{a}^0(\lambda, z_{AUV}) + \bar{b}_b^0(\lambda, z_{AUV}) - \bar{a}^0(490, z_{AUV}) - \bar{b}_b^0(490, z_{AUV})\right) \\ &\approx \frac{1}{\bar{\mu}_d}\left(\bar{a}^0(\lambda, z_{AUV}) - \bar{a}^0(490, z_{AUV})\right) \end{aligned} \quad (7)$$

Note that any component with a flat spectrum for the absorption or backscattering coefficient has no effect on $\delta\bar{K}_d^0(\lambda, z_{AUV})$, and hence in coastal waters, where large particles are present and $\bar{b}_b^0(\lambda)$ is rather flat (Morel and Maritorena 2001), this term may be omitted, even if it is not small compared to $\bar{a}^0(\lambda)$. The depth averaged total absorption, $\bar{a}^0(\lambda, z_{AUV})$, is the sum of the depth averaged absorption contributions from all constituents (as in Eq. 4), and thus allows the least squares inversion of $\delta\bar{K}_d^0(\lambda, z_{AUV})$ to obtain estimates of $\bar{a}_{ph}^0(522, z_{AUV})$ and $\bar{a}_{cm}^0(412, z_{AUV})$.

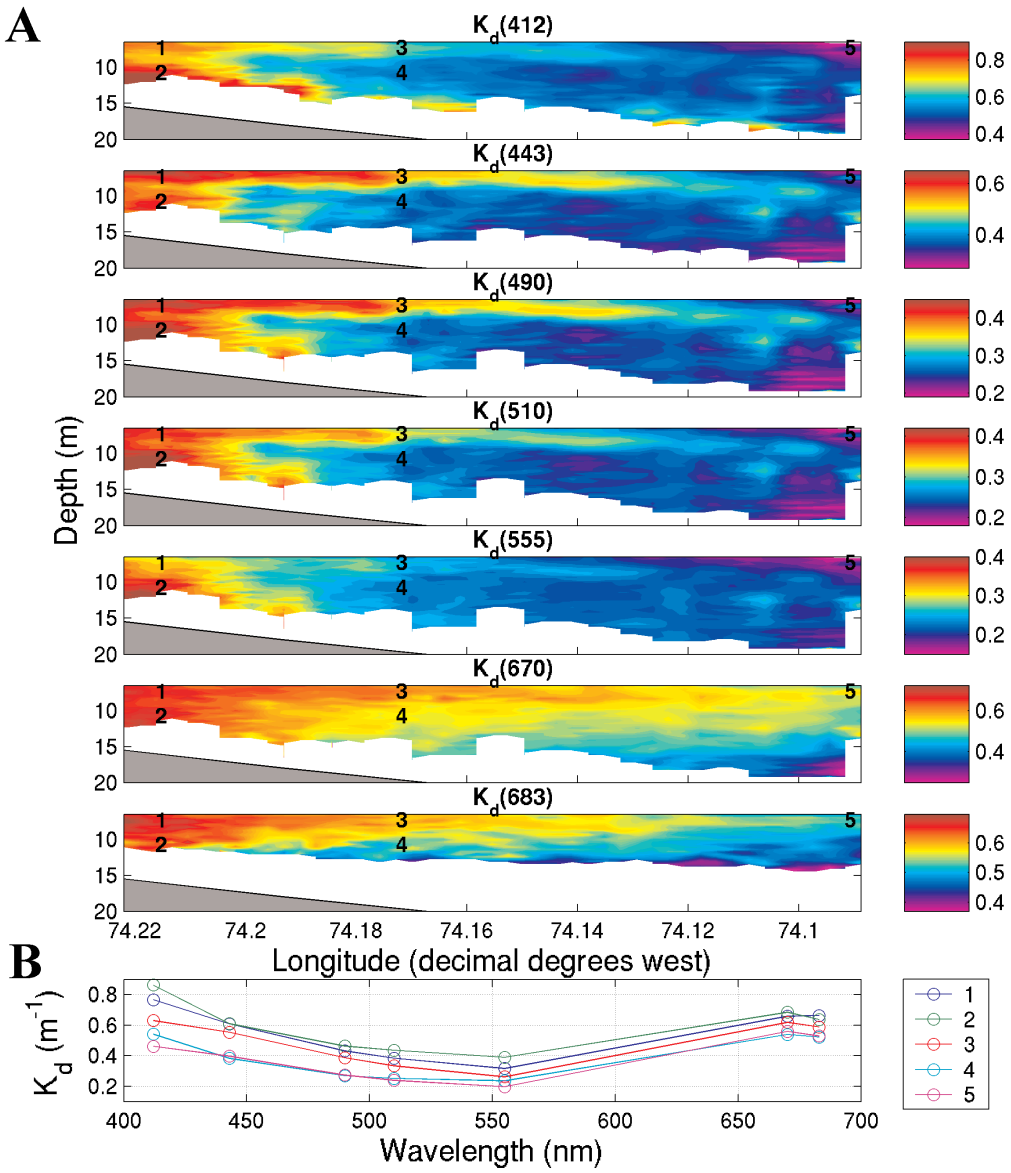

Fig. 3. Measured $K_d(\lambda,\bar{z})$ along the A-line transect. (A) Contour plots of measured $K_d(\lambda,\bar{z})$ in units of m^{-1}. (B) Spectra of $K_d(\lambda,\bar{z})$ corresponding to the numbered locations on the contour plots. Each value of $K_d(\lambda,\bar{z})$ is an averaged value for an approximately 1- to 3-m section of the water column. The estimates of $K_d(\lambda,\bar{z})$ were performed by linear regression of the log transformed $E_d(\lambda,z)$ data over 1- to 3-m depth intervals representing 30 $E_d(\lambda,z)$ measurements.

Method 3: Derivation of $\delta K_d(\lambda,\bar{z})$—When the AUV flight pattern has sufficiently long depth excursions, $\delta K_d(\lambda)$ can be computed over depth intervals as

$$\delta K_d(\lambda,\bar{z}) = K_d(\lambda,\bar{z}) - K_d(490,\bar{z}) = \frac{1}{\Delta z}\cdot\ln\left[\frac{E_d(490,z)}{E_d(\lambda,z)}\cdot\frac{E_d(\lambda,z+\Delta z)}{E_d(490,z+\Delta z)}\right] \quad (8)$$

where $\bar{z} = z + 1/2\cdot\Delta z$ is the depth assigned to $\delta K_d(\lambda)$ in our analysis. Using the same quality controls for irradiance described above for $K_d(\lambda,\bar{z})$, we obtained $\delta K_d(\lambda,\bar{z})$ by linear regression over 30 data points on the log transformed measurements. This is the approach followed by Nahorniak et al. (2001), except that we use a regression over several data points, whereas they used the ratio of two point measurements. The inversion is carried out with the same model as Eq. 7, except that the retrieved absorption values are now for small depth intervals (represented by $a_{ph}(522,\bar{z})$ and $a_{cm}(412,\bar{z})$).

Assessment

Study region and AUV deployment—During July 2000, REMUS deployments were conducted as part of the Office of Naval Research–sponsored Hyperspectral Coupled Ocean Dynamics

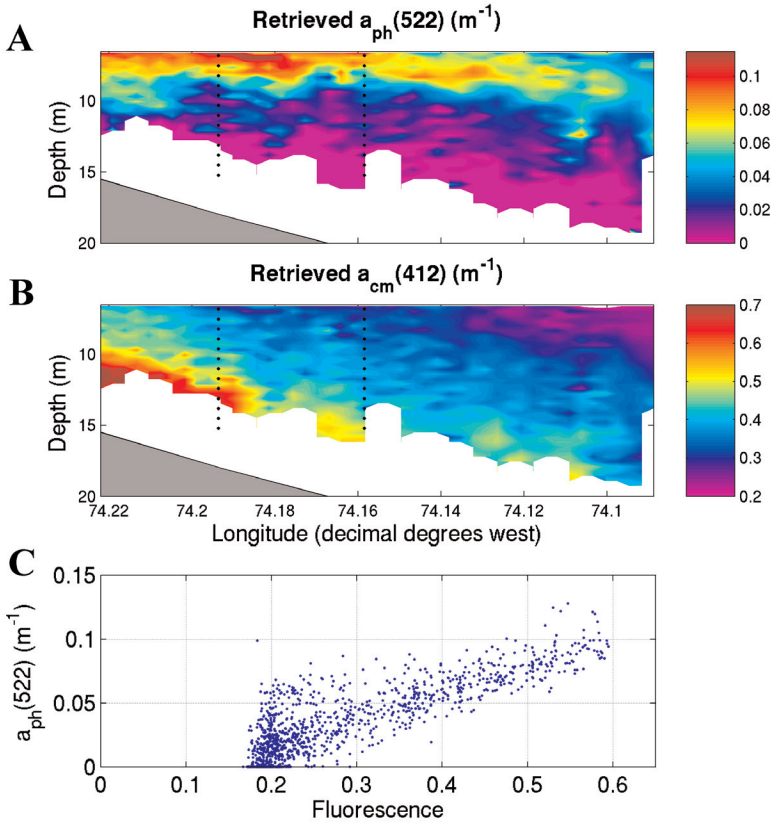

Fig. 4. Inverse model results for $K_d(\lambda,\bar{z})$ (Method 1) calculated over small depth intervals along the A-line transect and comparison to fluorescence. (A) Retrieved average absorption coefficient for phytoplankton ($a_{ph}(522,\bar{z})$; m^{-1}). (B) Retrieved absorption coefficient for nonalgal colored matter at 412 nm ($a_{cm}(412,\bar{z})$; m^{-1}). (C) Measured fluorescence versus $a_{ph}(522,\bar{z})$. The dotted lines on the contour plots indicate where vertical profiles of in situ IOPs were taken (*see* Figs. 5 and 6). For reference, using this spectrum $a_{ph}(412) = 2.1 \cdot a_{ph}(522)$ and $a_{ph}(490) = 1.7 \cdot a_{ph}(522)$.

Experiments (HyCODE; http://www.opl.ucsb.edu/hycode.html). The REMUS missions were conducted near the Long-term Ecosystem Observatory (LEO) on the New Jersey Shelf, USA. Fig. 1B shows a map of the LEO study region and some of the deployment paths that REMUS traveled in waters less than ~22 m deep. We present analyses for three deployments to illustrate the variability of physical and bio-optical properties in the study region: one along a straight transect (transect mode; 17 July 2000) and two that covered a radiator pattern (2-D mapping mode and 3-D mapping mode; 26 and 23 July 2000, respectively).

The transect mode involved deployment of the vehicle approximately 4 km offshore. Subsequent to the launch, the vehicle proceeded along a straight path in the horizontal (the 'A line' at the LEO site) and profiled the water column from a depth of 5 m to near the bottom (water depths varied from ~16 to 22 m), with a horizontal peak-to-peak distance of approximately 400 m. The minimal depth was selected to reduce the potential of collision with ships and buoys. This mode is used to map the vertical variations along the path, which for this experiment was approximately 20 km in horizontal extent.

The 2-D mapping mode was executed by transiting a radiator pattern while the vehicle was constrained to a near-constant depth of 3.0 ± 0.3 m, with cross-shore legs of 3 km alternating with along-shore legs of 100 m. The 3-D mapping mode allowed us to obtain resolution in both the vertical and horizontal because the depth of the vehicle undulated between 6 and 20 m while traveling a radiator pattern (cross-shore legs of 4 km alternating with along-shore legs of 420 m).

Next, we compare the three methods presented above by applying them to the irradiance measurements made in transect mode. Then, we apply Method 2, the only one applicable to the 2-D mapping mode. Lastly, we show the measured parameters for the 3-D mapping mode.

Transect mode, Method 1: Inversion of $K_d(\lambda,\bar{z})$ *to obtain* $a_{ph}(522,\bar{z})$ *and* $a_{cm}(412,\bar{z})$—This transect shows a clear stratification in the salinity and temperature measurements, with a pycnocline sloping from about 7 m nearshore to 10 m further offshore (Fig. 2). The pycnocline is a sharp vertical gradient in temperature and salinity that separates warm and fresh surface water from cold and salty bottom water. Fluorescence (Fig. 2C) shows a subsurface maximum east of 74.15°W near or just

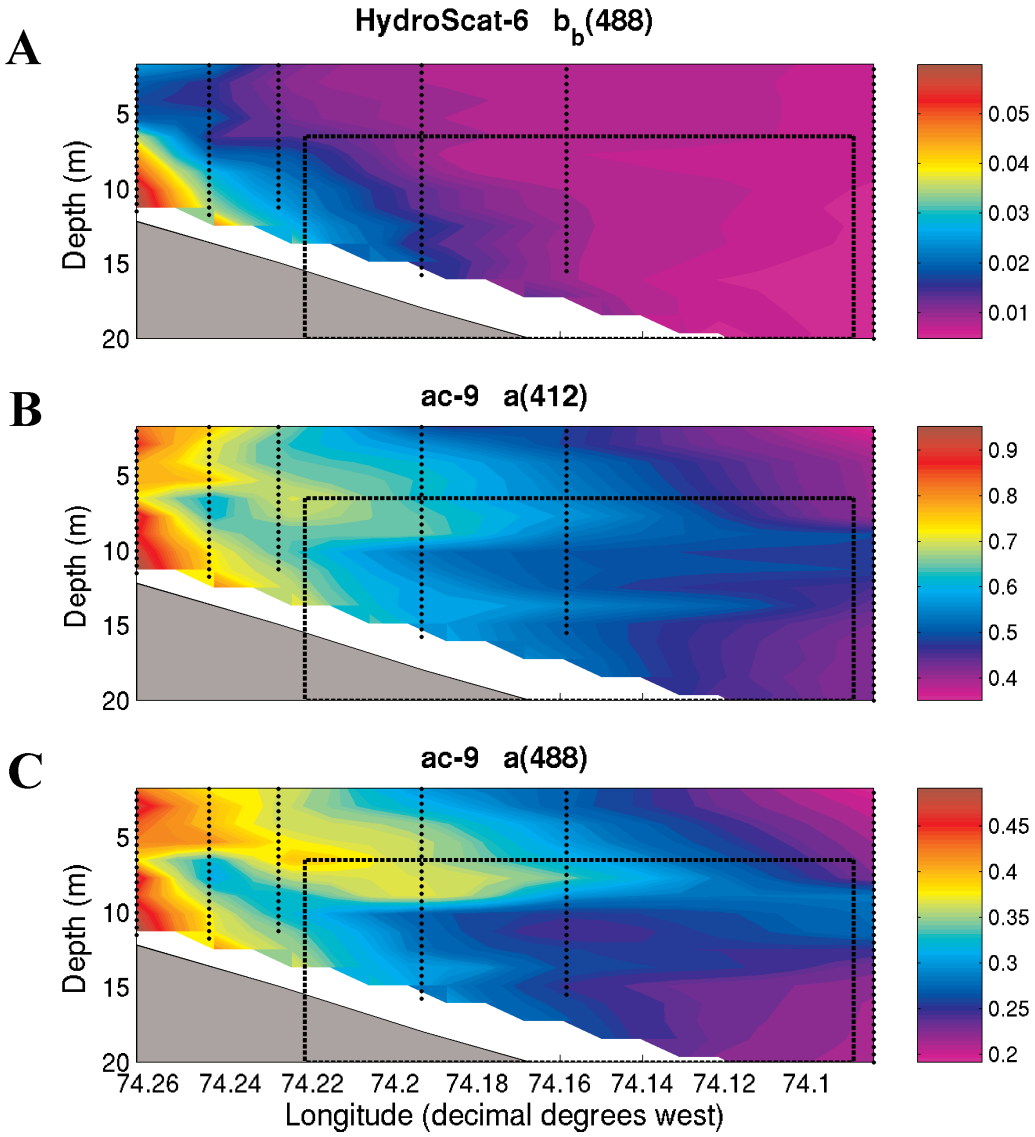

Fig. 5. Shipboard vertical profiles of in situ absorption and backscattering. Six vertical profiles with a HydroScat-6 (HOBI Labs) and ac-9 (WET Labs) were taken along the A-line transect ~3 h prior to the REMUS deployment. The black dotted lines show the cast locations (data provided by Trisha Bergmann). (A) Backscattering at 488 nm (m^{-1}) as measured with a HydroScat-6. (B) Absorption at 412 nm (m^{-1}) measured with an ac-9. (C) Absorption at 488 nm (m^{-1}) measured with an ac-9. The dashed lines create a rectangle indicating the range (longitude, depth) covered by REMUS, shown in all other plots for the transect mode.

above the pycnocline. The measurements of $K_d(\lambda,\bar{z})$ show a similar structure, with high values at the shallowest depth sampled nearshore (Fig. 3). This is particularly evident at 443 nm, where nearshore values are higher near the surface, and moving offshore, the maximal values slope down toward the pycnocline. Note that due to the high attenuation coefficient of water at long wavelengths, there are regions where $K_d(683,\bar{z})$ is not plotted at depth. Compared to the fluorescence data, it should be remembered that each value of $K_d(\lambda,\bar{z})$ is an averaged value for an approximately 1- to 3-m section of the water column whereas the fluorescence is effectively a point measurement. In addition, the fluorescence data are influenced in part by physiology (Kiefer and Reynolds 1992), whereas the attenuation measurement is directly related to absorption.

To demonstrate the need for an inversion algorithm applicable to Case 2 waters, we attempted to retrieve the concentration of chlorophyll (Chl, mg m^{-3}) using the statistical relationship developed by Morel and Maritorena (2001). This relationship is based on a large number of open ocean (Case 1) data and relates $K_d(\lambda)$ to a power function of the chlorophyll concentration. The patterns in the derived values of chlorophyll (not shown) for the offshore region were similar to those based on fluorometry but were very high at depth in nearshore waters, which is inconsistent with the fluores-

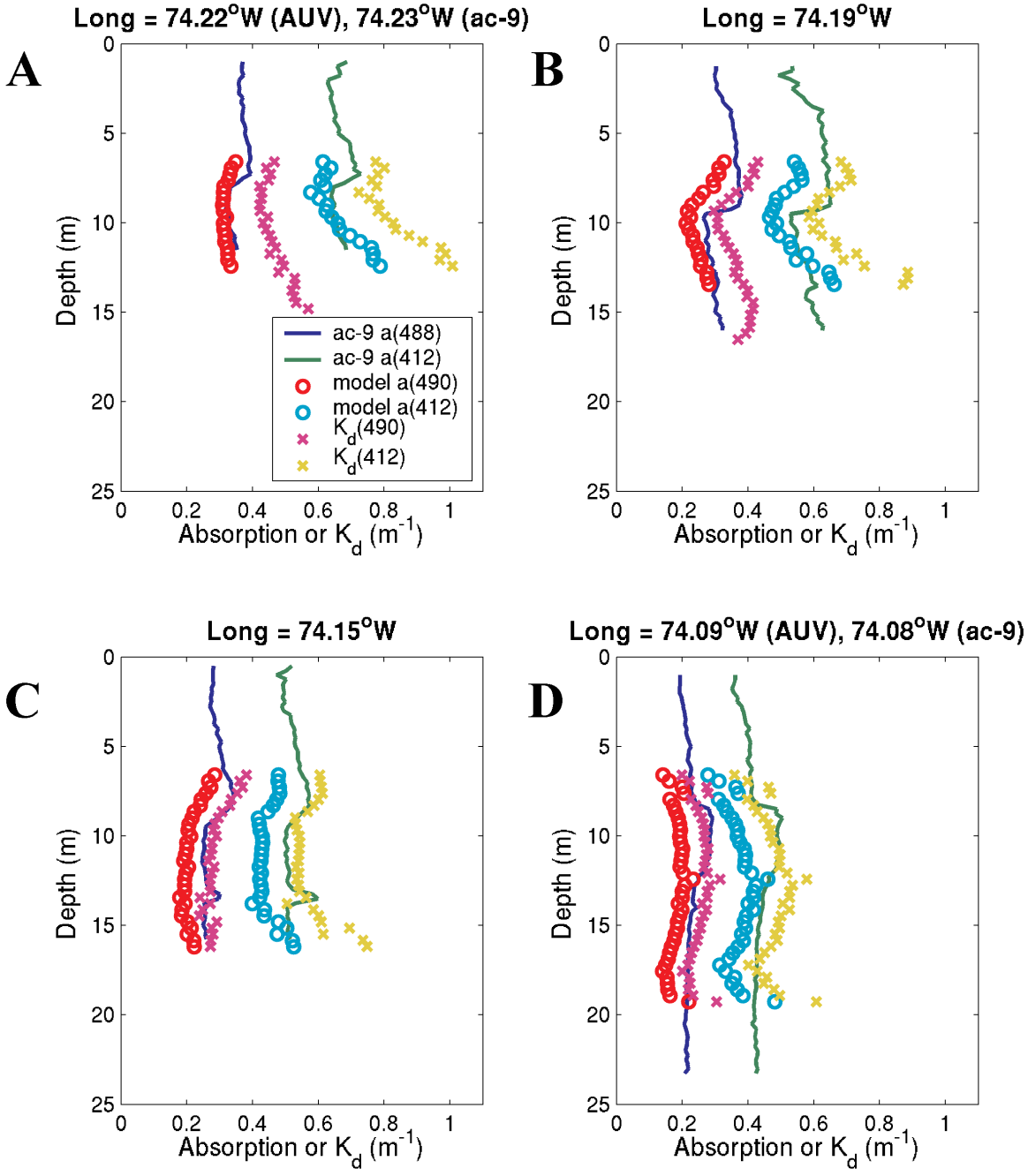

Fig. 6. Comparison of shipboard, inverse model, and AUV data. (A) The westernmost range of the AUV and a closely located ac-9 profile (*see* Fig. 5 for location of casts). (B) AUV and ac-9 at same location. (C) AUV and ac-9 at same location. (D) The easternmost range of the AUV and a closely located ac-9 profile. Profiles with an ac-9 were made ~3 h prior to the AUV deployment. The model retrieved absorption values that were calculated from $K_d(\lambda, \bar{z})$ are similar in vertical pattern and value to the in situ measurements by the ac-9.

cence data (Fig. 2C). This is not surprising as the optical conditions in these coastal waters are substantially different from those upon which the statistical relationship is based.

We then carried out the inversion analysis described above to create two-dimensional (longitude, depth) plots of the vertical variability in optical constituents (Fig. 4). The retrieved aver-

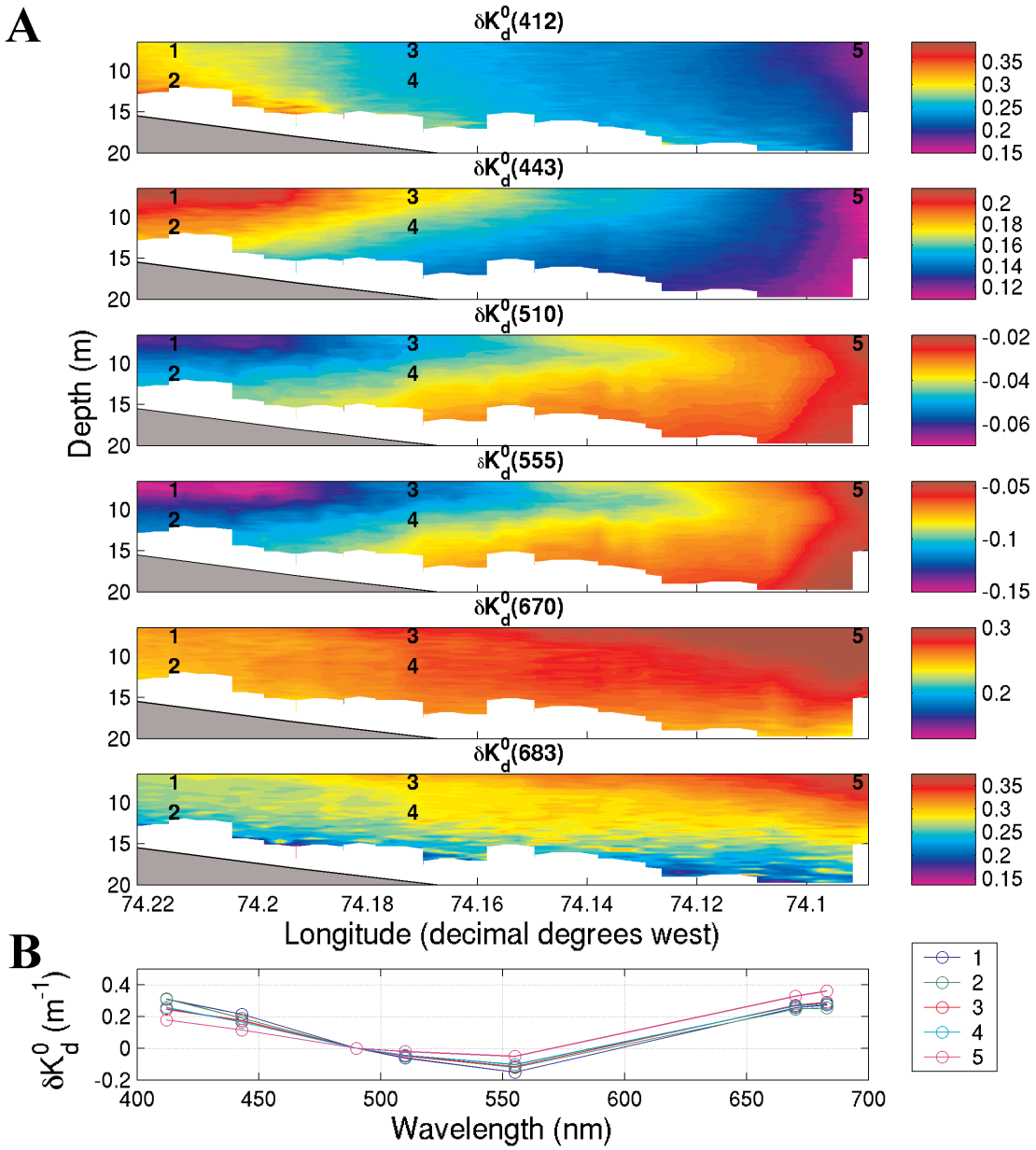

Fig. 7. Measured $\delta\bar{K}_d^0(\lambda, z_{AUV})$ along the A-line transect (Method 2). (A) Top six panels are contour plots of measured $\delta\bar{K}_d^0(\lambda, z_{AUV})$ in units of m^{-1}. (B) Bottom panel shows spectra of $\delta\bar{K}_d^0(\lambda, z_{AUV})$ corresponding to the numbered locations on the contour plots. The $\delta\bar{K}_d^0(\lambda, z_{AUV})$ method uses spectral ratios of irradiance measured at one depth and an assumed normalized spectrum of irradiance at the surface to compute absolute spectral differences in $\bar{K}_d^0(\lambda, z_{AUV})$, which is the average $K_d(\lambda)$ between the surface and the depth of the AUV.

age absorption coefficient for phytoplankton ($a_{ph}(522, \bar{z})$; Fig. 4A) closely resembles the fluorescence patterns observed (Fig. 2C). Note that in deep waters (i.e., >17 m) there are retrievals of $a_{ph}(522, \bar{z})$ = 0 by the inverse model. Shipboard measurements of absorption and backscattering were taken with an ac-9 (WET Labs) and HydroScat-6 (HOBI Labs), respectively, approximately 3 h prior to the AUV deployment (vertical profiles of inherent optical properties (IOP) data were provided by Trisha Bergmann pers. comm. 2003). Contour plots of the IOPs that were measured in situ show high absorption at 488 nm above ~8 m (Fig. 5C), whereas below ~5 m west of 74.18°W, an increase with depth in backscattering (Fig. 5A) and high $a(412)$ (Fig. 5B) were observed. The latter is consistent with the observed increase in nearshore colored matter absorption with depth that was retrieved by the inversion and suggests the resuspension of particulate matter from the sea bottom as found by Boss et al. (2003) and Chang et al. (2002). The total absorption values retrieved by the inverse model from the $K_d(\lambda, \bar{z})$ data show a close correspondence to in situ measurements of absorption (Fig. 6).

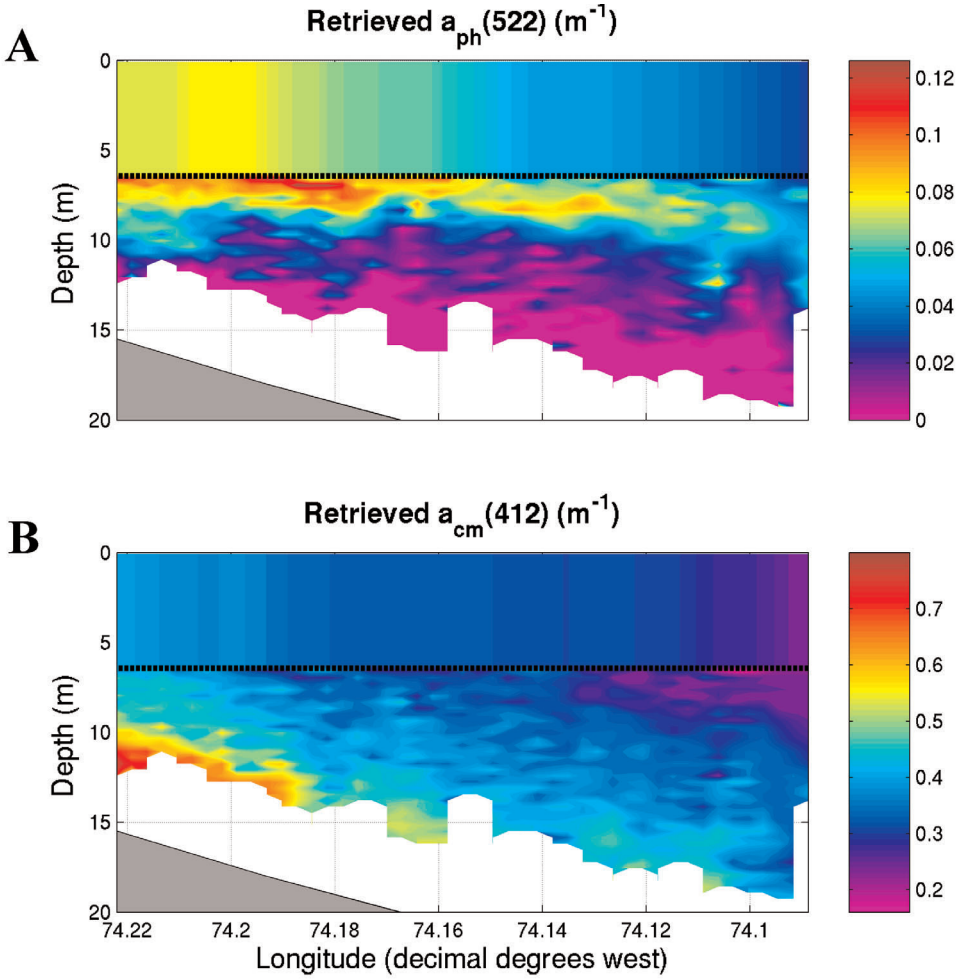

Fig. 8. Merging the inverse model results for $K_d(\lambda,\bar{z})$ (Method 1) and $\delta\bar{K}_d^0(\lambda,z_{AUV})$ (Method 2) along the A-line transect. (A) Retrieved absorption by phytoplankton at 522 nm ($a_{ph}(522,\bar{z})$ below dashed line and $\bar{a}_{ph}^0(522)$ above dashed line; m^{-1}). (B) Retrieved absorption by nonalgal colored matter at 412 nm ($a_{cm}(412,\bar{z})$ and $\bar{a}_{cm}^0(412,z_{AUV})$; m^{-1}). Above the dashed line, retrieved constituents from $\delta\bar{K}_d^0(\lambda,z_{AUV})$ are shown for z_{AUV} of 6.5 m (Method 2). It is an averaged measure of the constituents above this depth. Below the dashed line, retrieved constituents from $K_d(\lambda,\bar{z})$ are shown (Method 1).

Transect mode, Method 2: Inversion of $\delta\bar{K}_d^0(\lambda,z_{AUV})$ *to obtain* $\bar{a}_{ph}^0(522,z_{AUV})$ *and* $\bar{a}_{cm}^0(412,z_{AUV})$—Because the calculation of $\delta\bar{K}_d^0(\lambda,z_{AUV})$ provides an averaged measurement of attenuation from the surface of the water to the depth of measurement, the features in $\delta\bar{K}_d^0(\lambda,z_{AUV})$ (Fig. 7) appear quite different from those observed in the $K_d(\lambda,\bar{z})$ analysis (Fig. 3). In the $\delta\bar{K}_d^0(\lambda,z_{AUV})$ plots, the transition from higher attenuation coefficients at the surface to lower attenuation coefficients at depth is much smoother. Compared to the $K_d(\lambda,\bar{z})$ method described above, this calculation provides information about the average concentration of constituents in the water layer above the sensor. This can be shown by using the inverse model for $\delta\bar{K}_d^0(\lambda)$ to retrieve the average value of the absorption coefficient above 6.5 m (i.e., using the inversion at z_{AUV} = 6.5 m and assuming a constant value above that depth) and then merging this plot with the longitude-depth contours of absorption coefficients retrieved using absolute $K_d(\lambda,\bar{z})$ from 6.5 m to the depth restricted by light availability (Fig. 8; the dashed lines in Fig. 8 at 6.5 m correspond to the minimum depth of the fluorescence plot in Fig. 2). Note that the relative magnitude of $\bar{a}_{ph}^0(522,z_{AUV})$ above 6.5 m to $a_{ph}(522,\bar{z})$ below 6.5 m is consistent with the decrease in $a(488)$ observed in Fig. 5C above the shallowest sampling depth of the REMUS. The inversion of the $\delta\bar{K}_d^0(\lambda)$ profiles in terms of $\bar{a}_{ph}^0(522,z_{AUV})$ (Fig. 9) is broadly consistent with the observed patterns in the measured fluorescence (Fig. 2C), although an obvious smoothing with depth is observed in $\bar{a}_{ph}^0(522,z_{AUV})$ compared with the fluorescence measurement because it is a depth average. The absorption by nonalgal colored matter ($\bar{a}_{cm}^0(\lambda,z_{AUV})$) clearly follows the trends in the measured $\delta\bar{K}_d^0(412,z_{AUV})$ (Fig. 7), which is expected because $\delta\bar{K}_d^0(412,z_{AUV})$ will be affected mostly by dissolved colored matter in these coastal waters. The subtraction of $\bar{K}_d^0(490,z_{AUV})$ to obtain $\delta\bar{K}_d^0(412,z_{AUV})$ probably accounts for most of the variability in phytoplankton absorption. The $\delta\bar{K}_d^0(\lambda)$ technique allows the determination of the concentra-

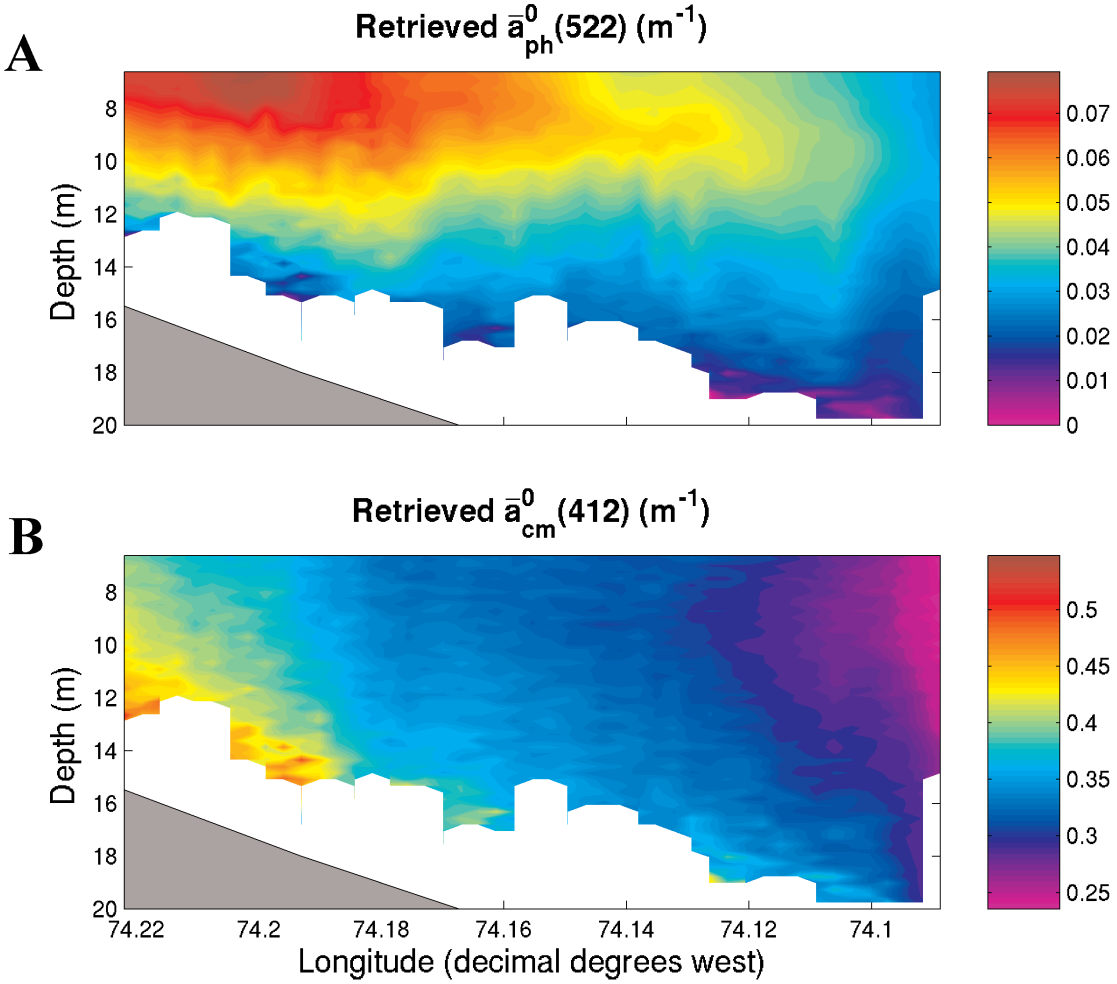

Fig. 9. Inverse model results for $\delta\bar{K}^0_d(\lambda, z_{AUV})$ along the A-line transect (Method 2). (A) Retrieved average absorption by phytoplankton ($\bar{a}^0_{ph}(522)$; m^{-1}). (B) Retrieved absorption by nonalgal colored matter at 412 nm ($\bar{a}^0_{cm}(412)$; m^{-1}).

tion of the constituents above the depth sampled and does not require any depth excursion (also *see* 2-D mapping mode, Method 2: Inversion of $\delta\bar{K}^0_d(\lambda, z_{AUV})$).

Transect mode, Method 3: Inversion of $\delta K_d(\lambda,\bar{z})$ *to obtain* $a_{ph}(522,\bar{z})$ *and* $a_{cm}(412,\bar{z})$—The $\delta K_d(\lambda,\bar{z})$ variations (Fig. 10) resemble the absolute measurements of $K_d(\lambda,\bar{z})$ (Fig. 3). The inversion of $\delta K_d(\lambda,\bar{z})$ (Fig. 11) provides a good correlation of the retrieved average absorption coefficient for phytoplankton ($a_{ph}(522,\bar{z})$) to measured fluorescence. However, below the pycnocline, the model retrieved many values of $a_{ph}(522,\bar{z})$ equal to 0. These are probably due to the assumptions that (1) the angular distribution of the light field (represented by $\bar{\mu}_d$) is constant with optical depth and independent of wavelength and (2) both the slope of the dissolved colored matter and the shape of the phytoplankton absorption spectra remain constant with depth. Given the limited number of wavebands available, it would be unrealistic to attempt the retrieval of a size factor for phytoplankton absorption or a slope for the nonalgal colored matter absorption. A more robust inverse model could be developed using numerical simulations of the light field to describe variations in $\bar{\mu}_d$ with optical depth and wavelength.

2-D mapping mode, Method 2: Inversion of $\delta\bar{K}^0_d(\lambda, z_{AUV})$—In this mode, the AUV remained at a constant depth. Temperature and salinity did not vary significantly over the area surveyed in mapping mode (not shown); however, ~20% variations in fluorescence were observed (Fig. 12).

A comparison of fluorescence as measured by the active fluorometer onboard the AUV and $\bar{a}^0_{ph}(522, z_{AUV})$ derived from the inverse model shows close correspondence (Fig. 12D). The correlation of estimated $\bar{a}^0_{ph}(522, z_{AUV})$ and measured fluorescence appears robust considering the narrow range of estimated $\bar{a}^0_{ph}(522, z_{AUV})$ and the different water masses sampled by each measurement (i.e., a "point measurement" versus an average between the surface and z_{AUV}). An advantage of the $\delta\bar{K}^0_d(\lambda, z_{AUV})$ approach is that it is insensitive to optical constituents whose effects on $K_d(\lambda,z)$ are spectrally flat. However, in the presence of high values of $b_b(\lambda,z)$, reconstruction to get

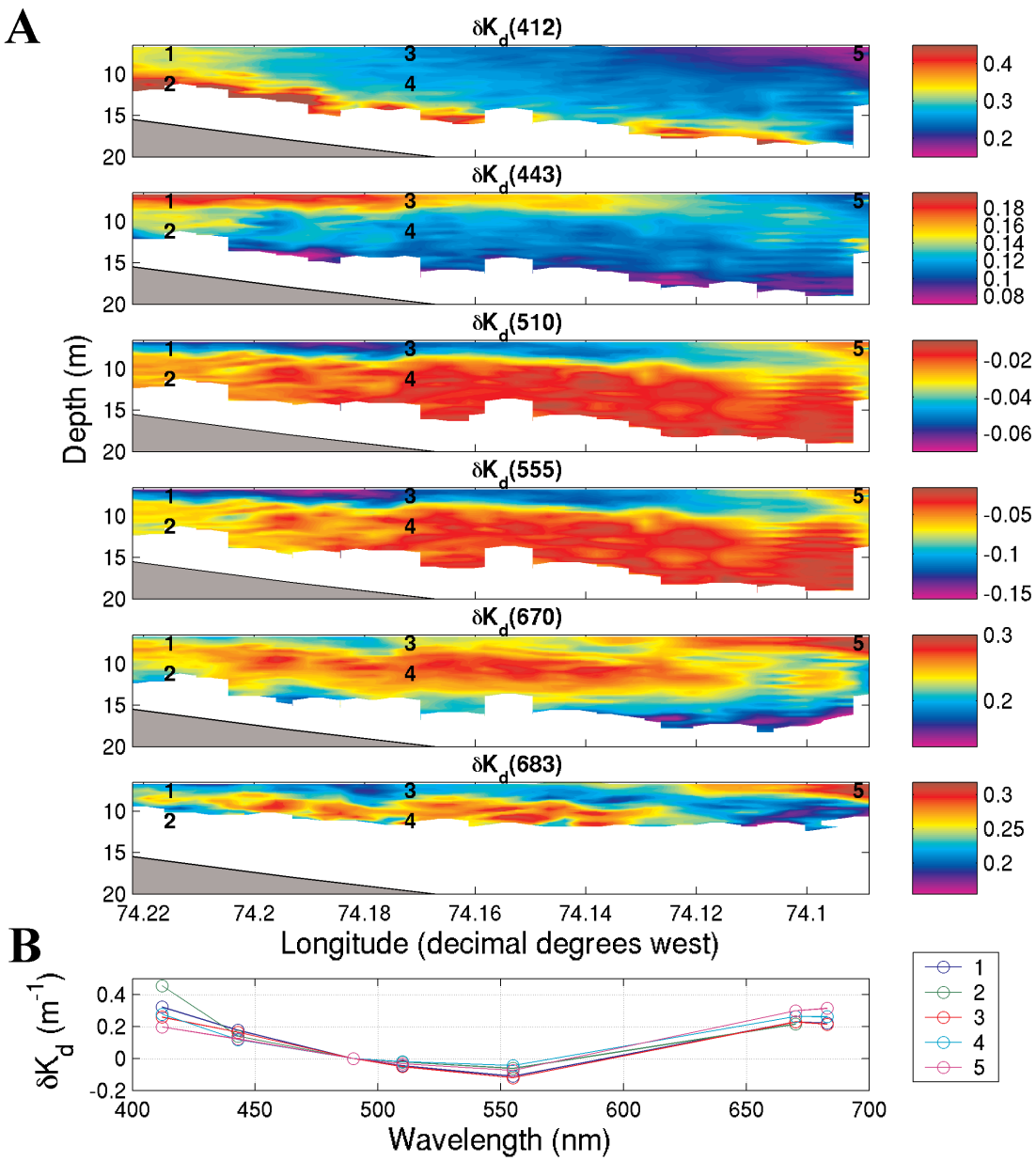

Fig. 10. Estimated $\delta K_d(\lambda,\bar{z})$ along the A-line transect (Method 3). (A) The top six panels are contour plots of measured $\delta K_d(\lambda,\bar{z})$ in units of m^{-1}. (B) The bottom panel shows spectra of $\delta K_d(\lambda,\bar{z})$ corresponding to the numbered locations on the contour plots. In the $\delta K_d(\lambda,\bar{z})$ method, spectral differences in $K_d(\lambda,\bar{z})$ are computed over 1- to 3-m depth intervals.

absolute values of $K_d(\lambda,z)$ using only retrieved absorption will lead to underestimates; in this study, $b_b(\lambda,z)$ values were low relative to absorption, and this was not an issue (Figs. 5 and 6).

3-D mapping mode: Calculation of $K_d(\lambda,\bar{z})$—The hydrographic and fluorometric measurements in 3-D mapping mode did not show significant horizontal variability, but had strong gradients in the vertical (Fig. 13). The lower light levels encountered on that day did not allow the use of the 412 nm downwelling irradiance channel such that separation into different absorbing constituents was not attempted. Instead a comparison of $K_d(443,\bar{z})$ with the fluorescence measurements, data shown in Fig. 13, suggest that phytoplankton were mostly influencing the variability in the absorption coefficient in this volume, or that nonalgal colored matter covaried strongly with phytoplankton biomass.

Discussion

We have demonstrated three approaches to retrieve the bio-optical properties of coastal waters using an AUV platform carrying an optical payload. The use of any particular method will be a function of the AUV sampling pattern and the light intensity at the sensor depth. All models retrieved proxies of phytoplankton absorption in the presence of high absorption by other compounds, without the requirement

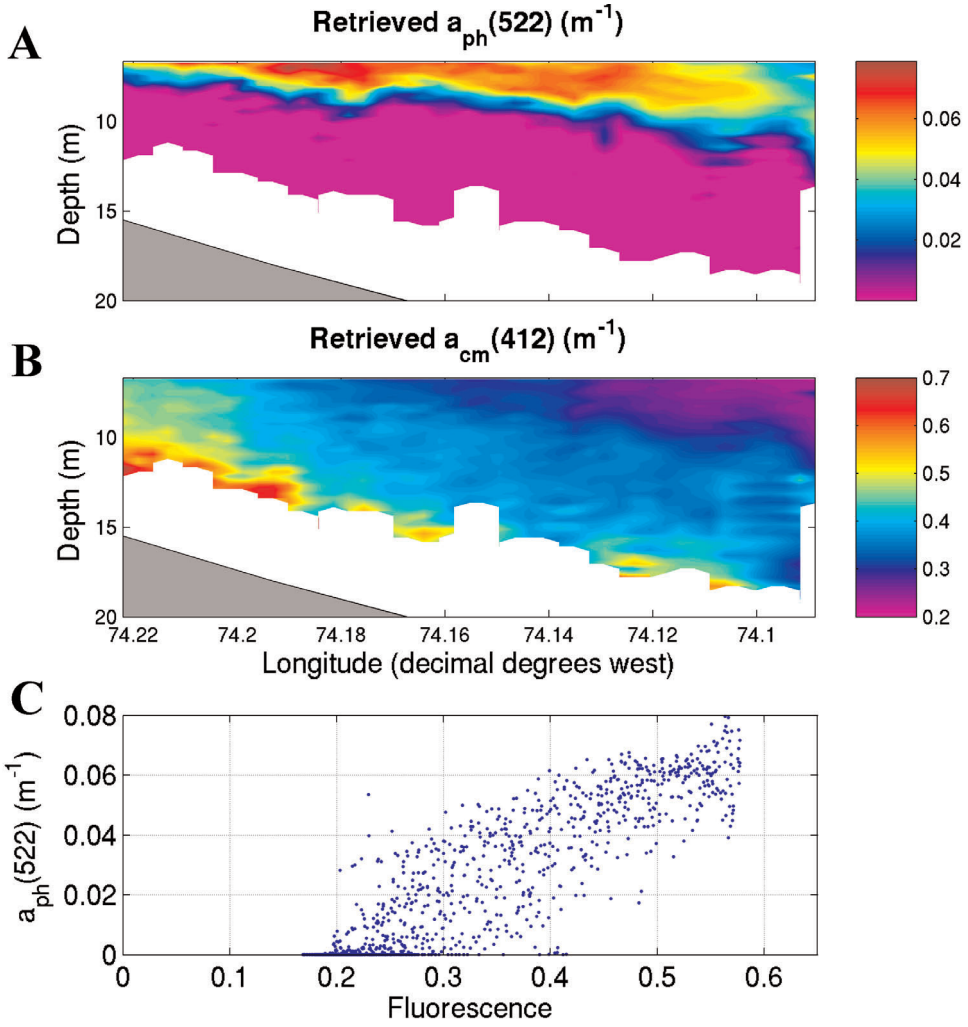

Fig. 11. Inverse model results for $\delta K_d(\lambda,\bar{z})$ along the A-line transect (Method 3) and comparison to fluorescence. (A) Retrieved average absorption coefficient for phytoplankton ($a_{ph}(522,\bar{z})$; m^{-1}). (B) Retrieved absorption coefficient for nonalgal colored matter at 412 nm ($a_{cm}(412,\bar{z})$; m^{-1}). (C) Measured fluorescence versus $a_{ph}(522,\bar{z})$.

of concurrent measurements with a surface sensor. In addition, the use of the $\delta\bar{K}_d^0(\lambda,z_{AUV})$ method with an assumed surface reference spectrum allowed the determination of the absorption properties above the sensor without any depth excursion by the sampling platform. In principle, this method is insensitive to changes in the magnitude, in contrast to spectral changes, in the incident solar irradiance spectrum. The estimates of $\bar{a}_{ph}^0(\lambda,z_{AUV})$ and $\bar{a}_{cm}^0(\lambda,z_{AUV})$ obtained with the inverse model are consistent with independent measurements taken in the same region and time period (not shown; laboratory spectrophotometric data for discrete water samples were provided by Mark Moline pers. comm. 2003).

Comments and recommendations

In this study, high-resolution underwater surveys of bio-optical properties show that the environmental characterization of the littoral ocean can be accurately conducted using an AUV platform outfitted with passive optical sensors. The lack of a surface reference for $E_d(\lambda)$, a major limitation for more conventional determinations of attenuation coefficients, is not a problem for the different approaches we have developed. Three-dimensional mapping is also feasible when the AUV undulates during a survey.

In contrast to previous methods for obtaining $K_d(\lambda,z)$, the $\delta\bar{K}_d^0(\lambda,z_{AUV})$ approach, which interprets changes in the shape rather than the magnitude of the irradiance spectrum, requires only measurements of downwelling spectral irradiance $E_d(\lambda)$ at a single depth to estimate the water constituents (i.e., absorption coefficient for phytoplankton and nonalgal colored matter). Consequently, a simple water quality instrument for monitoring $\bar{a}_{ph}^0(\lambda,z_{AUV})$ and $\bar{a}_{cm}^0(\lambda,z_{AUV})$ would only require E_d optical sensors (412, 443, 490, 510, and 555 nm) at one depth. We are presently exploring the possibility of a

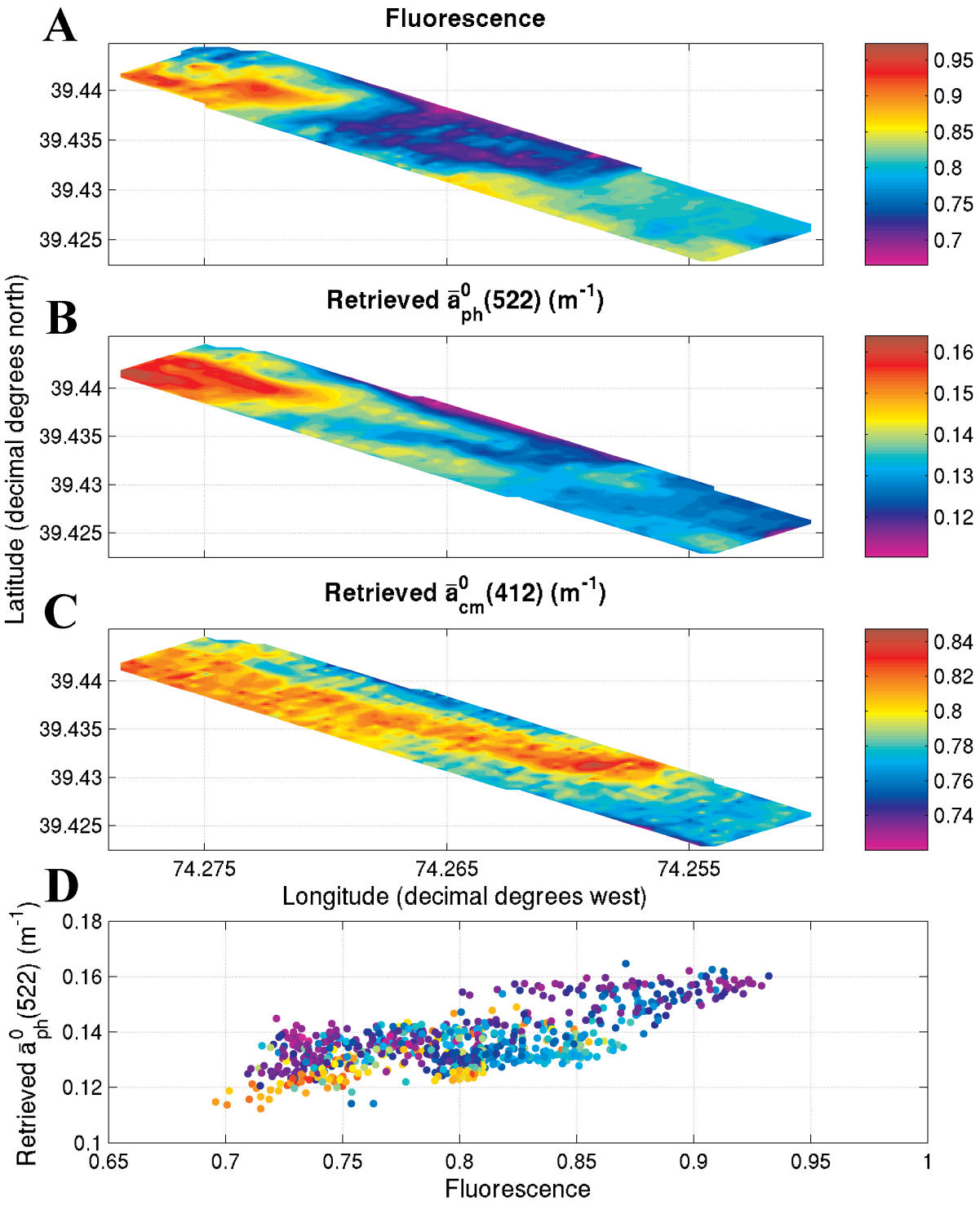

Fig. 12. Fluorescence and inverse model results (Method 2) for 2-D horizontal mapping mode survey by REMUS. (A) Fluorescence measured by the onboard fluorometer (normalized to the maximum value for all deployments). (B) Retrieved average absorption by phytoplankton ($\bar{a}^0_{ph}(522)$; m^{-1}). (C) Retrieved absorption by nonalgal colored matter at 412 nm ($\bar{a}^0_{cm}(412)$; m^{-1}). (D) Measured fluorescence versus $\bar{a}^0_{ph}(522)$ (normalized to the maximum value for all deployments). Red and orange colors on the scatter plot indicate higher incident irradiance at 490 nm. Longitude and latitude are in decimal degrees.

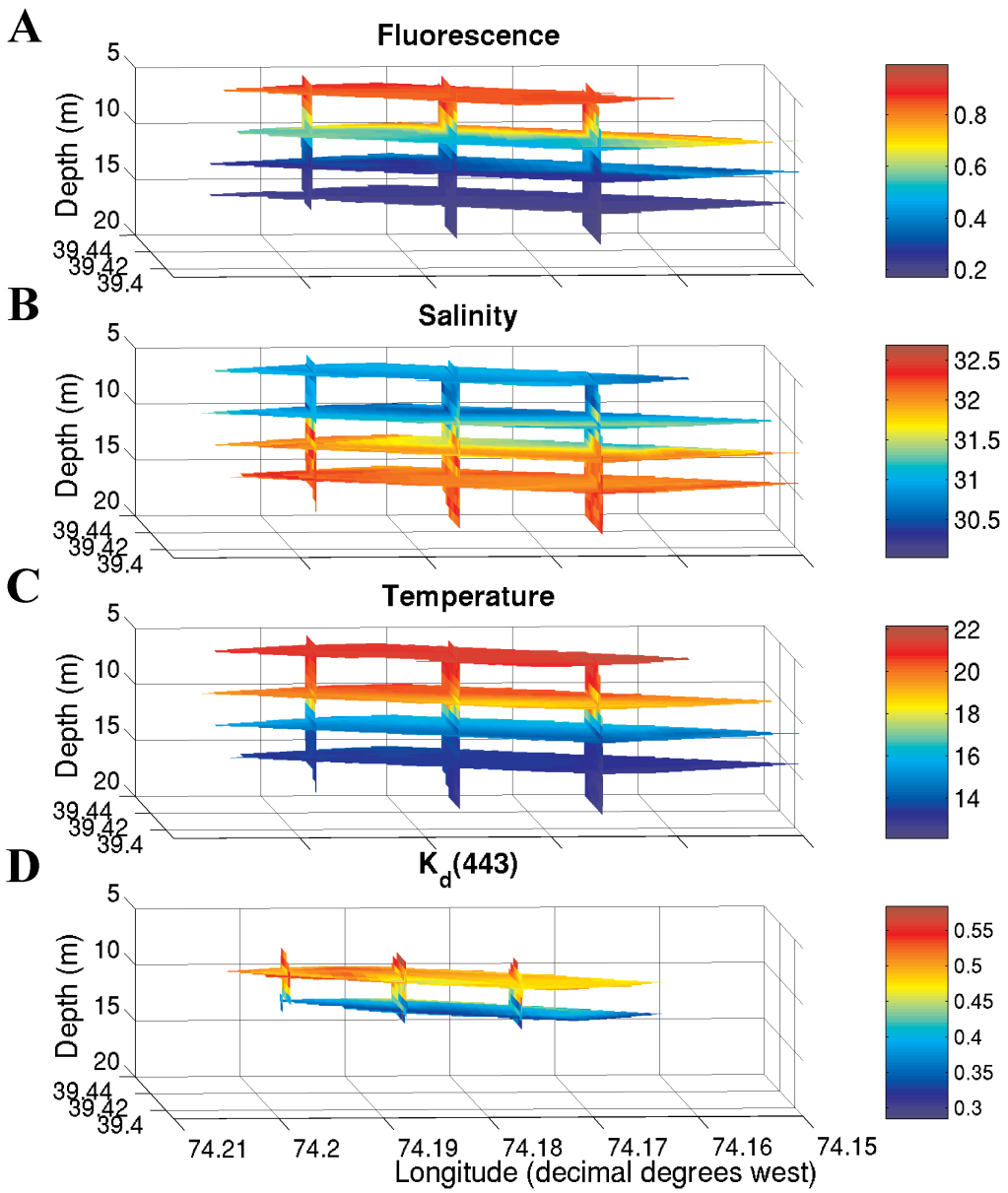

Fig. 13. Fluorescence, salinity, temperature, and $K_d(443,\bar{z})$ measured during 3-D mode survey by the instruments onboard REMUS. (A) fluorescence (normalized to the maximum value for all deployments) displayed as 3-D slices; (B) salinity; (C) temperature (°C); (D) $K_d(443,\bar{z})$ in units of m^{-1}. The axis going into the page is latitude in decimal degrees north.

smaller and more optimized number of bands. This method is transferable to other platforms such as Argo floats, profilers, gliders, and moorings.

References

Abbott, M. R., J. G. Richman, R. M. Letelier, and J. S. Bartlett. 2000. The spring bloom in the Antarctic Polar Frontal Zone as observed from a mesoscale array of bio-optical sensors. Deep-Sea Res. II 47:3285-3314.

Albert, A., and C. D. Mobley. 2003. An analytical model for subsurface irradiance and remote sensing reflectance in deep and shallow case-2 waters. Opt. Express 11:2873-2890.

Baker, K. S., and R. C. Smith. 1979. Quasi-inherent characteristics of the diffuse attenuation coefficient for irradiance, p. 60-63, SPIE: Ocean Optics VI.

Bartlett, J. S., A. M. Ciotti, R. F. Davis, and J. J. Cullen. 1998. The spectral effects of clouds on solar irradiance. J. Geophys. Res. 103:31017-31031.

Berwald, J., D. Stramski, C. D. Mobley, and D. A. Kiefer. 1998. Effect of Raman scattering on the average cosine and diffuse attenuation coefficient of irradiance in the ocean. Limnol. Oceanogr. 43:564-576.

Boss, E., W. S. Pegau, M. Lee, M. Twardowski, E. Shybanov, G. Korotaev, and F. Baratange. 2004. Particulate backscattering ratio at LEO 15 and its use to study particle composition and distribution. J. Geophys. Res. 109(C1): C01014 [doi: 10.1029/2002JC001514].

Bricaud, A., A. Morel, M. Babin, K. Allali, and H. Claustre. 1998. Variations of light absorption by suspended particles with the chlorophyll a concentration in oceanic (Case 1) waters: Analysis and implications for bio-optical models. J. Geophys. Res. 103:31033-31044.

Carder, K. L., F. R. Chen, Z. P. Lee, S. K. Hawes, and D. Kamykowski. 1999. Semianalytic moderate-resolution imaging spectrometer algorithms for chlorophyll *a* and absorption with bio-optical domains based on nitrate-depletion temperatures. J. Geophys. Res. 104:5403-5421.

Chang, G. C., and others. 2002. Nearshore physical processes and bio-optical properties in the New York Bight. J. Geophys. Res. 107(C9): 3133 [doi: 10.1029/2001JC001018].

Ciotti, A. M., M. R. Lewis, and J. J. Cullen. 2002. Assessment of the relationships between dominant cell size in natural phytoplankton communities and the spectral shape of the absorption coefficient. Limnol. Oceanogr. 47:404-417.

Coleman, T. F., and Y. Li. 1994. On the convergence of interior-reflective Newton methods for nonlinear minimization subject to bounds. Math. Program. 67:189-224.

——— and ———. 1996. An interior trust region approach for nonlinear minimization subject to bounds. SIAM J. Optimiz. 6:418-445.

Cullen, J. J., A. M. Ciotti, R. F. Davis, and M. R. Lewis. 1997. Optical detection and assessment of algal blooms. Limnol. Oceanogr. 42:1223-1239.

Dickey, T. D. 1991. The emergence of concurrent high-resolution physical and bio-optical measurements in the upper ocean and their applications. Rev. Geophys. 29:383-413.

——— and G. C. Chang. 2001. Recent advances and future visions: temporal variability of optical and bio-optical properties of the ocean. Oceanography 14:15-29.

Glenn, S. M., T. D. Dickey, B. Parker, and W. Boicourt. 2000. Long-term real-time coastal ocean observation networks. Oceanography 13:24-34.

Gordon, H. R. 1989. Can the Lambert-Beer law be applied to the diffuse attenuation coefficient of ocean water? Limnol. Oceanogr. 34:1389-1409.

Gregg, W. W., and K. L. Carder. 1990. A simple spectral solar irradiance model for cloudless maritime atmospheres. Limnol. Oceanogr. 35:1657-1675.

Griffiths, G. 2002. Technology and applications of autonomous underwater vehicles. Taylor and Francis.

Griffiths, G., R. Davis, C. Eriksen, D. Frye, P. Marchand, and T. Dickey. 2001. Towards new platform technology for sustained observations, p. 324-338. *In* C. J. Koblinsky and N. R. Smith [eds.], Observing the ocean for climate in the 21st century. GODAE, Bureau of Meteorology.

Kiefer, D. A., and R. A. Reynolds. 1992. Advances in understanding phytoplankton fluorescence and photosynthesis, p. 155–174. *In* P. G. Falkowski [ed.], Primary productivity and biogeochemical cycles in the sea. Plenum Press.

Kirk, J. T. O. 1994. Light and photosynthesis in aquatic ecosystems, 2nd ed. Cambridge Univ. Press.

Maritorena, S., A. Morel, and B. Gentili. 2000. Determination of the fluorescence quantum yield by oceanic phytoplankton in their natural habitat. Appl. Optics 39:6725-6737.

———, D. A. Siegel, and A. Peterson. 2002. Optimization of a semi-analytical ocean color model for global scale applications. Appl. Optics 41:2705-2714.

Marshall, B. R., and R. C. Smith. 1990. Raman scattering and in-water ocean optical properties. Appl. Optics 29:71-84.

Mitchell, B. G., M. Kahru, and J. Sherman. 2000. Autonomous temperature-irradiance profiler resolves the spring bloom in the Sea of Japan. Proc. Ocean Optics XV, Monaco.

Morel, A. 1988. Optical modeling of the upper ocean in relation to its biogenous matter content (Case I waters). J. Geophys. Res. 93:10749-10768.

——— and S. Maritorena. 2001. Bio-optical properties of oceanic waters: A reappraisal. J. Geophys. Res.-Oceans 106: 7163-7180.

Mueller, J. L., and G. S. Fargion. 2002. Ocean optics protocols for satellite ocean color sensor validation. Revision 3. Part 1., p. 137. NASA/TM-2002-21004/Rev3-Vol1. NASA Goddard Space Flight Center.

Nahorniak, J. S., M. R. Abbott, R. M. Letelier, and W. S. C. Pegau. 2001. Analysis of a method to estimate chlorophyll-*a* concentration from irradiance measurements at varying depths. J. Atmos. Ocean. Tech. 18:2063-2073.

Pope, R. M., and E. S. Fry. 1997. Absorption spectrum (380-700 nm) of pure water. II. Integrating cavity measurements. Appl. Optics 36:8710-8723.

Preisendorfer, R. W. 1976. Hydrologic optics. Vol. I. Introduction. U.S. Department of Commerce, National Oceanic and Atmospheric Administration, Environment Research Laboratory.

Purcell, M., C. von Alt, B. Allen, T. Austin, N. Forrester, R. Goldsborough, and R. Stokey. 2000. New capabilities of the REMUS autonomous underwater vehicle. OCEANS 2000 MTS/IEEE Conference and Exhibition.

Roesler, C., and E. Boss. 2003. Spectral beam attenuation coefficient retrieved from ocean color inversion. Geophys. Res. Lett. 30(9): 1468 [doi: 10.1029/2002GL016185].

——— and M. J. Perry. 1995. In situ phytoplankton absorption, fluorescence emission, and particulate backscattering spectra determined from reflectance. J. Geophys. Res. 100: 13279-13294.

Rudnick, D. L., and M. J. Perry. 2003. ALPS: Autonomous and Lagrangian Platforms and Sensors, Workshop Report, p. 64.

Siegel, D. A., T. K. Westberry, and J. C. Ohlmann. 1999. Cloud color and ocean radiant heating. J. Climate 12:1101-1116.

Sosik, H. M., R. E. Green, W. S. Pegau, and C. S. Roesler. 2001. Temporal and vertical variability in optical properties of

New England shelf waters during late summer and spring. J. Geophys. Res. 106:9455-9472.

Yu, X., T. Dickey, J. Bellingham, D. Manov, and K. Streilein. 2002. The application of autonomous underwater vehicles for interdisciplinary measurements in Massachusetts and Cape Cod Bays. Cont. Shelf Res. 22:2225-2245.

Zhang, X., M. R. Lewis, M. Li, B. Johnson, and G. Korotaev. 2002. The volume scattering function of natural bubble populations. Limnol. Oceanogr. 47:1273-1282.

Zheng, X., T. Dickey, and G. C. Chang. 2002. Variability of the downwelling diffuse attenuation coefficient with consideration of inelastic scattering. Appl. Optics 41:6477-6488.

Submitted 14 December 2003
Accepted 1 May 2004